CrossMark

J. Fluid Mech. (2018), *vol.* 854, *pp.* 367–419. © Cambridge University Press 2018
doi:10.1017/jfm.2018.638

Ventilated supercavitation around a moving body in a still fluid: observation and drag measurement

Jaeho Chung[1] **and Yeunwoo Cho**[1,†]

[1]Department of Mechanical Engineering, Korea Advanced Institute of Science and Technology, Yuseonggu, Daejeon, 34141, Republic of Korea

(Received 3 July 2017; revised 5 August 2018; accepted 7 August 2018; first published online 6 September 2018)

This experimental study examines ventilated supercavity formation in a free-surface bounded environment where a body is in motion and the fluid is at rest. For a given torpedo-shaped body and water depth (H), depending on the cavitator diameter (d_c) and the submergence depth (h_s), four different cases are investigated according to the blockage ratio ($B = d_c/d_h$, where d_h is the hydraulic diameter) and the dimensionless submergence depth ($h^* = h_s/H$). Cases 1–4 are, respectively, no cavitator in fully submerged ($B = 0$, $h^* = 0.5$), small blockage in fully submerged ($B = 1.5\,\%$, $h^* = 0.5$), small blockage in shallowly submerged ($B = 1.5\,\%$, $h^* = 0.17$) and large blockage in fully submerged ($B = 3\,\%$, $h^* = 0.5$) cases. In case 1, no supercavitation is observed and only a bubbly flow (B) and a foamy cavity (FC) are observed. In non-zero blockage cases 2–4, various non-bubbly and non-foamy steady states are observed according to the cavitator-diameter-based Froude number (Fr), air-entrainment coefficient (C_q) and the cavitation number (σ_c). The ranges of Fr, C_q and σ_c are $Fr = 2.6$–18.2, $C_q = 0$–6, $\sigma_c = 0$–1 for cases 2 and 3, and $Fr = 1.8$–12.9, $C_q = 0$–1.5, $\sigma_c = 0$–1 for case 4. In cases 2 and 3, a twin-vortex supercavity (TV), a reentrant-jet supercavity (RJ), a half-supercavity with foamy cavity downstream (HSF), B and FC are observed. Supercavities in case 3 are not top–bottom symmetric. In case 4, a half-supercavity with a ring-type vortex shedding downstream (HSV), double-layer supercavities (RJ inside and TV outside (RJTV), TV inside and TV outside (TVTV), RJ inside and RJ outside (RJRJ)), B, FC and TV are observed. The cavitation numbers (σ_c) are approximately 0.9 for the B, FC and HSF, 0.25 for the HSV, and 0.1 for the TV, RJ, RJTV, TVTV and RJRJ supercavities. In cases 2–4, for a given Fr, there exists a minimum cavitation number in the formation of a supercavity while the minimum cavitation number decreases as the Fr increases. In cases 2 and 3, it is observed that a high Fr favours an RJ and a low Fr favours a TV. For the RJ supercavities in cases 2 and 3, the cavity width is always larger than the cavity height. In addition, the cavity length, height and width all increase (decrease) as the σ_c decreases (increases). The cavity length in case 3 is smaller than that in case 2. In both cases 2 and 3, the cavity length depends little on the Fr. In case 2, the cavity height and width increase as the Fr increases. In case 3, the cavity height and width show a weak dependence on the Fr. Compared to case 2, for the same Fr, C_q and σ_c, case 4 admits a double-layer supercavity instead of a single-layer supercavity. Connected with this behavioural observation, the body-frontal-area-based drag

† Email address for correspondence: ywoocho@kaist.ac.kr

https://doi.org/10.1017/jfm.2018.638 Published online by Cambridge University Press

coefficient for a moving torpedo-shaped body with a supercavity is measured to be approximately 0.11 while that for a cavitator-free moving body without a supercavity is approximately 0.4.

Key words: cavitation, drops and bubbles

1. Introduction

If a body moves in a gas, then the frictional drag would be lower than that of the same body moving in a liquid because the frictional drag depends on the dynamic viscosity of a fluid. For example, the viscosity of water is approximately one hundred times larger than that of air. In addition, if there exists a fore–aft pressure difference which is proportional to the fluid density, the pressure drag or the form drag on a body in a gas also would be lower than that of the same body moving in a liquid. For example, the density of water is approximately one thousand times larger than that of air. Therefore, during its motion, if a body is completely enveloped in a single large gaseous cavity, the associated total drag is expected to be significantly reduced. This phenomenon is known as supercavitation. Thus, the creation and maintenance of supercavitation have been of great interest in naval applications such as a high-speed underwater vehicle, air lubrication of a ship hull, a high-speed torpedo etc. (Ceccio 2010). The most relevant dimensionless number in the study of supercavitation is the cavitation number,

$$\sigma_c = \frac{2(p_r - p_c)}{\rho V^2}, \tag{1.1}$$

where p_r is a reference or a background pressure, p_c is the cavity pressure, ρ is the density of the surrounding liquid and V is the relative speed between the body and the surrounding liquid. In wetted flows (absent any cavity), the relevant dimensionless number is the pressure coefficient $C_p = 2(p_x - p_r)/\rho V^2$, where p_x is the local pressure at a specific location. Therefore, in cavity flows, $\sigma_c = -C_p$. A relatively small cavitation number is more favourable for supercavitation; a relatively high-speed natural supercavitation and a relatively low-speed ventilated supercavitation. Many similarities exist between a natural supercavitation and a ventilated supercavitation. For example, the sizes of both types of cavities scale with the cavitation number in approximately the same way. Outside of the time-averaged cavity shapes, however, the physics are quite different. This is especially true when one begins to look at the cavity dynamics. Given the fact that the fundamental physics regarding the time-averaged cavity shapes are the same for both types of supercavitation, many previous experimental studies have been done on ventilated supercavitation instead of a natural one which is more difficult to achieve or to definitively observe in laboratory environments (Logvinovich 1972; Epshtein 1973; Hrubes 2001; Spurk & König 2002; Schaffar *et al.* 2005; Cameron *et al.* 2011). Furthermore, many prior studies on ventilated supercavitation have been done exclusively in closed water-circulation tunnels rather than open environments (Self & Ripken 1955; Cox & Clayden 1956; Schauer 2003; Kawakami 2010; Zhou *et al.* 2010; Haipeng *et al.* 2014; Nouri *et al.* 2015; Karn *et al.* 2016). In these kinds of closed water-tunnel studies, various steady-state supercavity formations or cavity-closure modes have been

https://doi.org/10.1017/jfm.2018.638 Published online by Cambridge University Press

observed based on some representative dimensionless numbers; the cavitation number σ_c in (1.1), and the Froude number

$$Fr = \frac{V}{\sqrt{gd_c}}, \tag{1.2}$$

the air-entrainment coefficient

$$C_q = \frac{Q}{d_c^2 V}, \tag{1.3}$$

and the blockage ratio

$$B = \frac{d_c}{d_h}; \quad d_h = \frac{4A_c(\text{cross-sectional area})}{P(\text{wetted perimeter})}. \tag{1.4}$$

Here, g is the gravitational acceleration, d_c is the diameter of the disk-type cavitator, Q is the ventilated gas volumetric flow rate and d_h is the hydraulic diameter of a tunnel. Well-known examples of steady-state cavity formations are the foamy cavity, twin-vortex supercavity (Cox & Clayden 1956; Kawakami 2010; Zhou *et al.* 2010), quad-vortex supercavity (Kapankin & Gusev 1984; Kawakami & Arndt 2011), reentrant-jet supercavity (Gadd & Grant 1965; Skidmore 2013) and pulsating supercavity (Silberman & Song 1961; Song 1961; Karlikov *et al.* 1987; Semenenko 2001*a*; Semenenko 2001*b*; Skidmore 2013). These different supercavity formations are quantitatively differentiated according to certain relationships between some of dimensionless parameters Fr, σ_c, C_q and B, depending on separate studies. An axisymmetric reentrant-jet supercavity occurs when the Fr is high or when the gravitational force is negligible compared to the inertia force. The twin-vortex supercavity occurs when the Fr is low or when the gravity effect is not negligible any more. In these kinds of closed or bounded environments, the blockage effect always exists, which favours the occurrence of the twin-vortex supercavity rather than the reentrant-jet supercavity (Karn *et al.* 2016). Karn *et al.* (2016) posit that the closure mechanism is mainly determined by the pressure difference across the gas–water interface at the cavity closure. For the reentrant-jet (RJ) supercavity, the pressure difference is dominated by the momentum of the reentrant water jet, while for a twin-vortex (TV) supercavity, such a difference is much smaller. Based on the liner momentum theorem, they suggest a formula showing that the pressure difference monotonically decreases as the blockage ratio increases or *vice versa*. Therefore, in a closed environment, a higher blockage (B) leads to a smaller pressure difference, promoting the occurrence of a twin-vortex supercavity. Comparatively, in unbounded environments, the blockage effect from a wall does not exist. Therefore, with no dependence on the blockage ratio, the open-environment supercavity formation will depend only on the Froude number, the cavitation number and the air entrainment coefficient. In a free-surface environment, the blockage effect may be small but finite; thus, the associated blockage ratio can be similarly defined to that of a closed environment. Therefore, in this case, the various types of supercavity formations will depend on the cavitation number (1.1), the Froude number (1.2), the air-entrainment coefficient (1.3) and the blockage ratio (1.4). Moreover, various types of supercavity formations may depend on the closeness of a body to the free surface and the existence of a body, which are dimensionlessly represented, respectively, by

$$h^* = \frac{h_s}{H}, \tag{1.5}$$

https://doi.org/10.1017/jfm.2018.638 Published online by Cambridge University Press

$$d^* = \frac{d_c}{d} = \begin{cases} \text{finite (body)} \\ \infty \text{ (no body)}, \end{cases} \tag{1.6}$$

where h_s is the submergence depth of a body, H is the water depth, d is the diameter of the body and d_c is the diameter of the cavitator. For example, six parameters (1.1)–(1.6) will determine the shape of a reentrant-jet (RJ) type supercavity which can be approximated as an ellipsoid with a length (l), a width (w) and a height (h) or dimensionlessly with reference to a cavitator diameter d_c,

$$l^* = \frac{l}{d_c}, \tag{1.7}$$

$$w^* = \frac{w}{d_c}, \tag{1.8}$$

$$h^* = \frac{h}{d_c}. \tag{1.9}$$

In addition, for each type of supercavity formation, the drag coefficient (C_d) based on the frontal area of a moving body can be measured and compared to a non-supercavitating moving body according to the body-diameter-based Reynolds number (Re_d).

$$C_d = \frac{F_D}{\frac{1}{2}\rho V^2 \left(\frac{\pi}{4} d^2\right)} \tag{1.10}$$

$$Re_d = \frac{\rho V d}{\mu}, \tag{1.11}$$

where, F_D is the drag force, ρ is the density of a liquid and μ is the dynamic viscosity of a liquid. To the best of the present authors' knowledge, all these themes have not been well addressed in previous experimental studies in free-surface environments, although there have been a few relevant experimental studies (Campbell & Hilborne 1958; Kuklinski *et al.* 2001). Campbell & Hilborne (1958) conducted experiments on the formation of steady-state RJ and TV supercavities in a circular free-surface water channel (water depth: 0.46 m, channel width: 0.91 m, submergence depth: 0.22 m) with disk-type cavitators (diameter: 0.013 m, 0.019 m, 0.025 m, corresponding blockage ratio $B = 1.4\,\%$, $2.1\,\%$, $2.8\,\%$ for $h^* = 0.47$). Kuklinski *et al.* (2001) did experiments on the dynamics of ventilated supercavitation in a straight free-surface channel (water depth: 3.6 m, channel width: 7.3 m, no information about the submergence depth) with a disk-type cavitator ($B = 2\,\%$) and cone-type cavitators. The theme of Campbell & Hilborne's (1958) work is closer to that of the present experimental study. They showed that an RJ supercavity occurs when $\sigma_c Fr > 1$, and a TV supercavity occurs when $\sigma_c Fr < 1$ (which will be shown not to agree with the present study). For the case of $B = 3\,\%$ for $h^* = 0.5$ in the present study, we observe diverse supercavities, which were not observed in their work for a similar condition $B = 2.8\,\%$ and $h^* = 0.47$. In addition, they did not consider the effect of the closeness of the free surface on the formation of supercavities. Therefore, these are the subjects of the present paper. From the towing tank experiment with a free-surface environment, we observe different types of supercavity formations at steady state depending on the cavitation number (1.1), the Froude number (1.2), the air-entrainment coefficient (1.3), the blockage ratio (1.4), the closeness of a

https://doi.org/10.1017/jfm.2018.638 Published online by Cambridge University Press

body to the free surface (1.5) and the existence of a body (1.6). In particular, for a reentrant-jet type supercavity, we measure the ellipsoidal shape in terms of the dimensionless length, width and height (1.7)–(1.9) in the following form.

$$\frac{l}{d_c}, \frac{w}{d_c}, \frac{h}{d_c} = fcn\left(Fr, C_q, \sigma_c, B, \frac{d_c}{d}, \frac{h_s}{H}, Re_d\right). \tag{1.12}$$

In addition, for each type of supercavity formation, we measure the drag coefficient (1.10) based on the frontal area of a moving body,

$$C_d = fcn\left(Fr, C_q, \sigma_c, B, \frac{d_c}{d}, \frac{h_s}{H}, Re_d\right) \tag{1.13}$$

and, therefore, estimate the amount of drag reduction compared to a non-supercavitating moving body according to the body-diameter-based Reynolds number (Re_d). As a simple check of (1.12) and (1.13) in view of dimensional analysis, because we have fourteen dimensional parameters (ρ, μ, h_s, d_c, V, Q, p_c, d, g, $H(d_h)$, l, w, h, F_d), there will be $14-3=11$ dimensionless parameters, where the number of independent dimensional parameters is three in terms of their dimensions.

In the next section § 2, the detailed experimental set-up and procedures are explained. In the experiment, depending on the ratio of the size of the cavitator to that of the body (1.6), the blockage ratio (1.4) and the closeness of a body to the free surface (1.5), four different cases are considered both when a body exists ($d \neq 0$ in (1.6)) behind a cavitator and three different cases when a body does not exist ($d = 0$ in (1.6)) behind a cavitator. As will be shown, both cases result in almost the same results in terms of steady-state phenomena including supercavity formation. In other words, the dimensionless parameter $d^* = d_c/d$ (1.6) is excluded from the parameter space. In § 3, for each case, observation of various steady-state phenomena, including supercavity formation, are presented depending on the variation of the relevant dimensionless parameters. In the present work, the role of viscosity (μ) or the Reynolds number (Re_d) is not included in supercavity formation. Dimensional parameters are the volumetric flow rate, the body speed and the resultant pressure behind the moving body (cavity pressure in the case of supercavity formation). The former two are the independent variables before each test and the latter is the dependent variable after each test. The equivalent dimensionless parameters are the Froude number, the air-entrainment coefficient and the cavitation number (for the existence of a cavity) or the pressure coefficient (in the absence of a cavity) where the relevant length scale is the diameter of the cavitator or the body depending on the existence of a cavitator. Then, for example, for a reentrant-jet type supercavity, their dimensionless lengths, widths, and heights are measured according to the following dimensionless parameters, neglecting the effects of d_c/d and Re_d.

$$\frac{l}{d_c}, \frac{w}{d_c}, \frac{h}{d_c} = fcn\left(Fr, C_q, \sigma_c, B, \frac{h_s}{H}\right), \tag{1.14}$$

which are compared with existing theoretical and semi-empirical results. Finally, in § 4, the associated drags of the various steady states in § 3 are measured and compared with each other according to the Reynolds numbers based on the body diameter, from which the effect of supercavitation on the drag reduction can be clearly seen. The drag coefficient can be expressed as follows, neglecting the effect of d_c/d.

$$C_d = fcn\left(Fr, C_q, \sigma_c, B, \frac{h_s}{H}, Re_d\right). \tag{1.15}$$

https://doi.org/10.1017/jfm.2018.638 Published online by Cambridge University Press

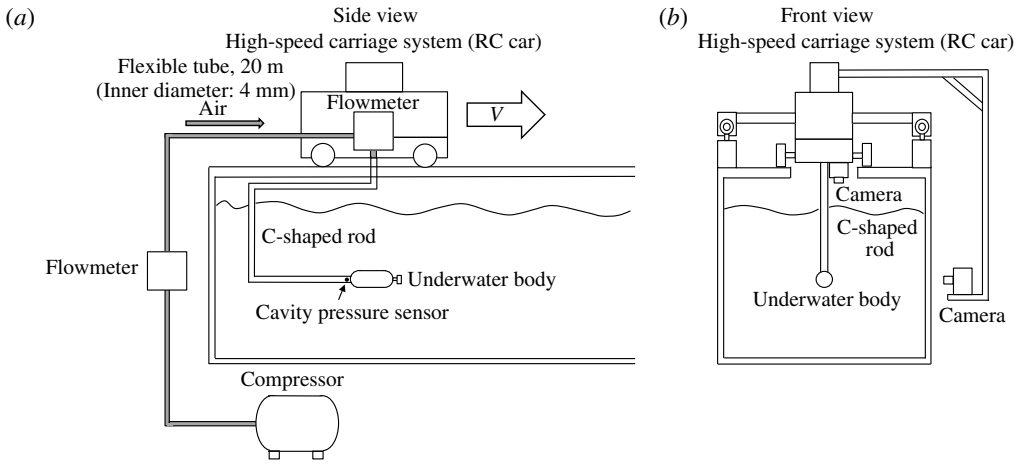

FIGURE 1. Schematics of the experimental set-up ((*a*) side view, (*b*) front view).

2. Experimental set-up

To make observations of the supercavitation phenomenon around a moving underwater body in a still fluid, a specialized towing water tank was designed and installed, as shown in schematics of figure 1. The tank size is 19.2 m long, 1 m wide and 1 m high and the side walls of the tank are made of transparent glass for visual observation from the outside. The towing system is a combination of a remodelled battery-driven remote control (RC) car and two straight rails which are laid on the two sides atop and along the entire length of the water tank. The RC car can run with a maximum speed of 7 m s^{-1} along the rails, and the RC car and the underwater body are rigidly attached to each other through a right-angled C-shaped connecting rod, and, thus, the underwater body is driven by the RC car with the same speed. The use of the right-angled C-shaped rod (diameter: 10 mm) is to minimize the influence of the rod on the flow and the cavity formation around the moving underwater body. In the test, the speed range is 1–7 m s^{-1}, therefore the relevant Reynolds number based on the rod diameter is between 10 000 and 70 000. In this flow regime, there is a laminar boundary layer separation at 80° and the associated wake is completely turbulent with a vortex shedding (Panton 2005; Sumer & Fredsoe 2010). Regardless of this vortex shedding, we checked that the whole C-shaped rod/stinger mount system is sufficiently rigid to prevent the vibration of a body to which a cavitator is attached. We checked our image data using pixels for the rigidity of the body. Most of the time at the steady state during a running test, the variation of the movement is very difficult to identify even from the pixel test. There are some rare intermittent moments only during the acceleration and the deceleration, however, in which the body moves less than 1 pixel. Since our 1 pixel corresponds to 4.7 mm, the movement is less than 4.7 mm. Therefore, considering the body length (90 mm), the relative movement is less than $4.7/90 = 5.2\,\%$ at worst, only during the acceleration and deceleration. The speed of the RC car or the underwater body is digitally controlled and varied from 1 to 7 m s^{-1} at steady state in the experiment (figure 2). The time interval of a steady state depends on the speed of the RC car due to the finite length of the tank; with each target constant speed in mind, first, the position of the underwater body is identified according to time from the video-recording data (figure 2*a*). For all cases, the driving distance is

https://doi.org/10.1017/jfm.2018.638 Published online by Cambridge University Press

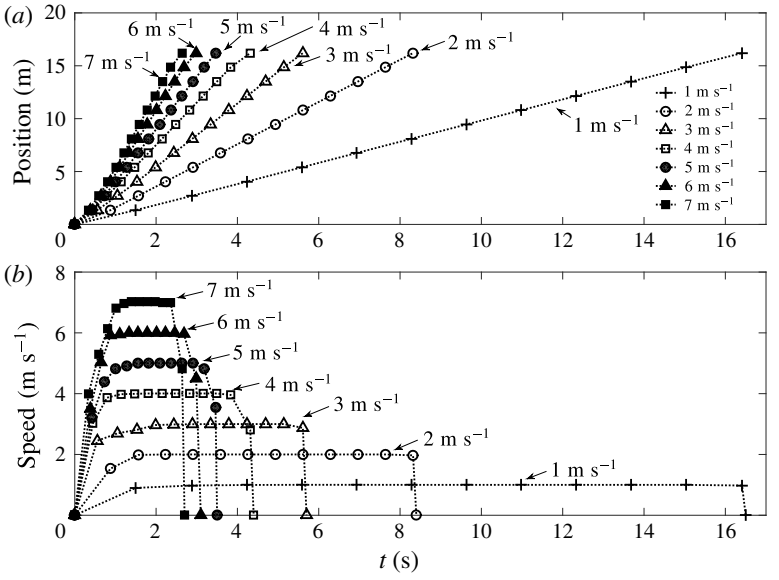

FIGURE 2. Position and speed of the underwater body versus time. (*a*) Position versus time, (*b*) speed versus time.

17.5 m. Then, the instantaneous speed of the moving body is obtained by calculating the slope of two consecutive position data during a corresponding time interval (figure 2*b*). In figure 2(*b*), one can see three phases; the accelerating phase, the constant-speed phase and the decelerating phase. Low-speed cases have relatively longer accelerating and constant-speed phases compared to the high-speed cases. In particular, for constant-speed observations, we have time of approximately 15 s for the case of 1 m s^{-1} and approximately 1 s for the case of 7 m s^{-1}. We set-up seven speeds 1, 2, 3, 4, 5, 6, 7 m s^{-1} due to the limitation of the tank length. We checked that the digitally controlled speed of the RC car show almost zero input–output discrepancy and almost zero variation from the target speed at steady state. For the real-time observation of supercavity formation around the moving underwater body, two video-recording cameras (Sony HDR-AS100V, 240 fps, 800 × 480 pixels) are attached to the towing system as shown in figure 1. The camera near the tank wall is for the side view observation of supercavitation and that at the bottom of the RC car is for the top view observation of supercavitation. For the video recording of the clear side view observation, black papers are glued to the opposite side of the tank wall to minimize the reflection of light. For the present ventilated supercavitation experiment, as mentioned in the introduction, the important dimensionless number is the cavitation number or the relative underpressure of the cavity,

$$\sigma_c = \frac{2(p_r - p_c)}{\rho V^2} = \frac{2(p_{atm} + \rho g h_s - p_c)}{\rho V^2}, \tag{2.1}$$

where h_s is the submergence depth of the centre of the moving body from the free surface. The cavity pressure p_c is measured using a film-type pressure sensor (Teksan FlexiForce A201, Operation range: 39 000–163 700 Pa at −40–60 °C, nonlinearity error < ±3 % F.S., repeatability error < ±2.5 % F.S., hysteresis error < ±4.5 % F.S.,

https://doi.org/10.1017/jfm.2018.638 Published online by Cambridge University Press

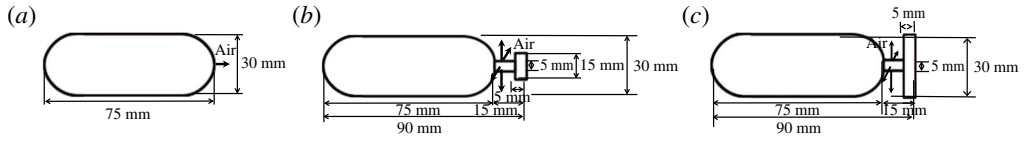

FIGURE 3. Torpedo-shaped (cylinder capped with hemispherical ends) underwater bodies (weight: 140 g) (*a*) without a cavitator, (*b*) with a small disk-type cavitator (diameter: 15 mm, weight: 15 g), (*c*) with a large disk-type cavitator (diameter: 30 mm, weight: 22 g).

drift error $< \pm 1.3\,\%$ F.S., response time < 5 μs), which is attached to the surface of the C-shaped rod behind the body and is completely inside the cavity once the supercavity is formed. Figure 3 shows the details of the bodies with or without a disk-type cavitator. The baseline underwater body is designed in the form of a torpedo (a cylinder capped with hemispherical ends) and is made of aluminium. The body size is 75 mm long, and 30 mm in diameter (figure 3*a*), which is thicker than the diameter of the supporting rod (10 mm). Thus, one may suspect that the resultant phenomena may be different from those in cases without a body. However, as will be shown in the subsequent section § 3, it turns out that the existence of a body has little influence on the flow pattern and the cavity shape, thus showing the almost same phenomena as those in cases without a body. A disk-shaped cavitator is prepared, which can be attached to or detached from the nose of the body, to investigate how its existence affects the formation of a supercavity. The radius of the cavitator is 15 mm (figure 3*b*) or 30 mm (figure 3*c*). For the case without a cavitator, the pressurized air is ejected from the hole at the nose of the underwater body (figure 3*a*). For the case with a cavitator, the pressurized air is ejected from four equally spaced holes drilled on the periphery of the straight aluminium pipe connecting the cavitator and the underwater body (figure 3*b*,*c*). During the test, the centre of the underwater body is positioned 0.25 m or 0.085 m below the water's surface with water depth 0.5 m, so that the pressure around the underwater body is very close to the atmospheric pressure (0.10375 MPa for 0.25 m, 0.10213 MPa for 0.085 m). For the realization of natural supercavitation, the local pressure should be dropped close to be the vapour pressure $P_v = 2340$ Pa at room temperature (20 °C). Then, the speed of the moving body should be at least approximately 45 m s^{-1} from a conservative calculation based on the cavitation number $\sigma_v = 2(p_r - p_v)/\rho V^2 \approx 0.1$ (Kawakami 2010; Kawakami & Arndt 2011). As will be shown in section § 3, ventilated supercavitation also occurs with a cavitation number ($\sigma_c = 2(p_r - p_c)/\rho V^2$) around 0.1. In the preliminary test, due to the short length of the towing water tank (19.2 m) and the low value of the maximum speed (7 m s^{-1}) of the moving underwater body available in the current experimental setting, we could not observe any cavity formation near the nose of the moving underwater body. Literature has shown that the time-averaged shape of a supercavity is a function of the cavitation number and the Froude number, neither of which depends upon the actual composition of the gaseous phase. For natural (vaporous) supercavitation, $p_c = p_v$, which requires speeds much higher than those achievable in the present facility to achieve a value of σ_c sufficiently small to result in a supercavity. Ventilation using pressurized air allows small values of σ_c, to be achieved at much lower speeds by increasing the cavity pressure p_c. The ventilation system is basically a simple compressor which blows pressurized air with the maximum gauge pressure of 0.6 MPa at the compressor outlet. The pressurized air

https://doi.org/10.1017/jfm.2018.638 Published online by Cambridge University Press

flows through a flexible thin tube (inner diameter: 4 mm, length: 20 m) which starts from the compressor outlet, via air flowmeters (SMC Flow switches PFM710-C6-A, Operation range: 0.2–10 l min^{-1}; PFM725-C6-A, Operation range: 0.5–25 l min^{-1}; PFM750-C6-A, Operation range: 1–50 l min^{-1}; PFM711-C6-A, Operation range: 2–100 l min^{-1}, all repeatability error $< \pm 1\,\%$, F.S.), and ends at the nose of the moving underwater body, wherein the thin tube goes into the hole of the rear side of the body and reaches the hole of the front side of the body (figures 1 and 3). The air flowmeter is used to measure the ejected volume flow rate of air, and there is no noticeable variation according to time in the reading during the whole time of a single test. In the next section § 3, the main results are expressed in terms of Fr, C_q and σ_c. These dimensionless parameters are obtained from the measured dimensional quantities V, Q and p_c. As described, the speed V is digitally controlled and shows almost zero error. The error related to already mentioned Q (repeatability error $< \pm 1\,\%$ F.S.) is machine originated and the error related to p_c is measurement originated and we checked that the time variations of Q and p_c during a steady state are almost zero during each test. We produce three kinds of plots, Fr versus C_q diagram for various σ_c, Fr versus σ_c diagram for various C_q, C_q versus σ_c diagram for various Fr. The single data point in each diagram is obtained from at least three tests and the $\pm 1\,\%$ repeatability error bars (F.S.) are included for C_q data and measurement error bars are included for σ_c data. Also, for the measurement of the length, width and height of a reentrant-jet supercavity, we include error bars since the measurement was carried out based on the pictures taken from at least three identical tests. Between each single test, an approximately 10 minute break was always given for the motion of water to become calm in the water tank where a wave/current absorber was installed at both end walls. In more detail, after a single test, we observed that it took approximately 3–5 minutes for the water surface to become calm and for the fluctuating velocities within the body of the tank to become completely dissipated, which were checked by our visual observation and by the camera-recorded data. Further, to be sure of a near zero-turbulence initial condition, we waited for an additional 5 minutes before the next test.

3. Experimental results

Our interest is in the supercavity formation with a resultant different cavity pressure (p_c) around the moving body with different steady-state speeds (V) for various cases depending on the existence of a cavitator, the cavitator size (d_c) and the submergence depth (h_s). In table 1, for a given body size (diameter: d) and water depth (H), four different cases are categorized according to the dimensionless cavitator size ($d^* = d_c/d$), the blockage ratio ($B = d_c/d_h$) and the dimensionless submergence depth ($h^* = h_s/H$); $d^* = 0$ (no cavitator), 0.5 (small cavitator), 1 (large cavitator), $B = 0$, 1.5 %, 3 % and $h^* = 0.17$ (shallowly submerged), 0.5 (fully submerged). The words ‘fully submerged’ and ‘shallowly submerged’ are used to represent the ‘no-wave’ cases (cases 2 and 4) and ‘wave-like disturbance’ case (case 3) on the free surface, respectively, during the steady-state cavity formation while the body is moving. These words are not used to represent ‘deep water’ or ‘shallow water’ conditions. In the wave-like disturbance case (case 3), all the conditions are ‘deep water’ conditions. As will be shown in § 3.2.3 for case 3, for an RJ-type supercavity near the free surface, the cavity length is approximately 10 to 33 times the diameter of the cavitator ($d_c = 15$ mm). Therefore, the length of the crest-like disturbance on the free surface, which is comparable to the length of the cavity, is approximately 150 to 495 mm.

https://doi.org/10.1017/jfm.2018.638 Published online by Cambridge University Press

Case	Cavitator/body size	Blockage ratio	Submergence depth
	$d^* = d_c/d$ $(d = 30$ mm$)$	$B = d_c/d_h$	$h^* = h_s/H$
1	$d^* = 0$ (no cavitator)	$B = 0$	Fully submerged $h^* = 0.5$
2	$d^* = 0.5$ (small cavitator)	$B = 1.5\,\%$	Fully submerged $h^* = 0.5$
3	$d^* = 0.5$ (small cavitator)	$B = 1.5\,\%$	Shallowly submerged $h^* = 0.17$
4	$d^* = 1$ (large cavitator)	$B = 3\,\%$	Fully submerged $h^* = 0.5$

TABLE 1. Four experimental conditions; d is the diameter of the body, d_c is the diameter of the cavitator, H is the water depth, W is the channel width, d_h is the hydraulic diameter of the channel and h_s is the submergence depth.

Assuming the disturbance wavelength is approximately twice the cavity length, then the wavelength (λ) would be 300 to 990 mm. Since the water depth $H = 500$ mm, one can conclude that the deep-water condition $H > \lambda/2$ (150–495 mm) is always satisfied. The hydraulic diameter (d_h) of the channel with a free surface in the calculation of the blockage ratio B is

$$d_h = \frac{4\ (\text{area})}{\text{wetted perimeter}} = \frac{4HW}{2H + W}, \tag{3.1}$$

where W is the channel width (1 m) in the present study. Cases 1–4 are, respectively, (d^*, B, h^*) = (0, 0 %, 0.5), (0.5, 1.5 %, 0.5), (0.5, 1.5 %, 0.17), (1, 3 %, 0.5). When there is no body ($d^* = \infty$), table 2 shows three cases 5, 6 and 7 which correspond to cases 2, 3 and 4 in table 1, i.e. (d^*, B, h^*) = (∞, 1.5 %, 0.5), (∞, 1.5 %, 0.17), (∞, 3 %, 0.5). In the comprehensive tests for all conditions, we found that the effect of the existence of a body (d^*) on the resultant cavity formation is not important. Examples are shown in figures 4–6 which are the comparisons between cases 2 and 5, between cases 3 and 6 and between cases 4 and 7, respectively. As shown, for the same set of (Fr, C_q, σ_c), the results are almost the same between cases 2 and 5, between cases 3 and 6 and between cases 4 and 7. Therefore, only cases 1–4 in table 1 will be considered since we are also interested in the drag reduction of a supercavitating moving body compared to a non-supercavitating moving body. Hereafter, all the experimental results except case 1 are expressed in terms of three dimensionless numbers; the cavitator-diameter-based Froude number Fr (1.2), the cavitator-diameter-based air-entrainment coefficient C_q (1.3) and the cavitation number σ_c (2.1). For case 1 (no cavitator), the body-diameter-based Froude number (Fr_d), the body-diameter-based air-entrainment coefficient ($C_{q,d}$) and the cavitation number (σ_c) will be used, where

$$Fr_d = \frac{V}{\sqrt{gd}}, \tag{3.2}$$

$$C_{q,d} = \frac{Q}{d^2 V}, \tag{3.3}$$

since $d_c = 0$ makes Fr and C_q singular for a finite value of V.

3.1. *Overall transient to steady-state phenomena*

As an example of case 2 in table 1, figure 7 shows the video-recording image data for the whole process of supercavitation around a body with a 15 mm diameter cavitator

https://doi.org/10.1017/jfm.2018.638 Published online by Cambridge University Press

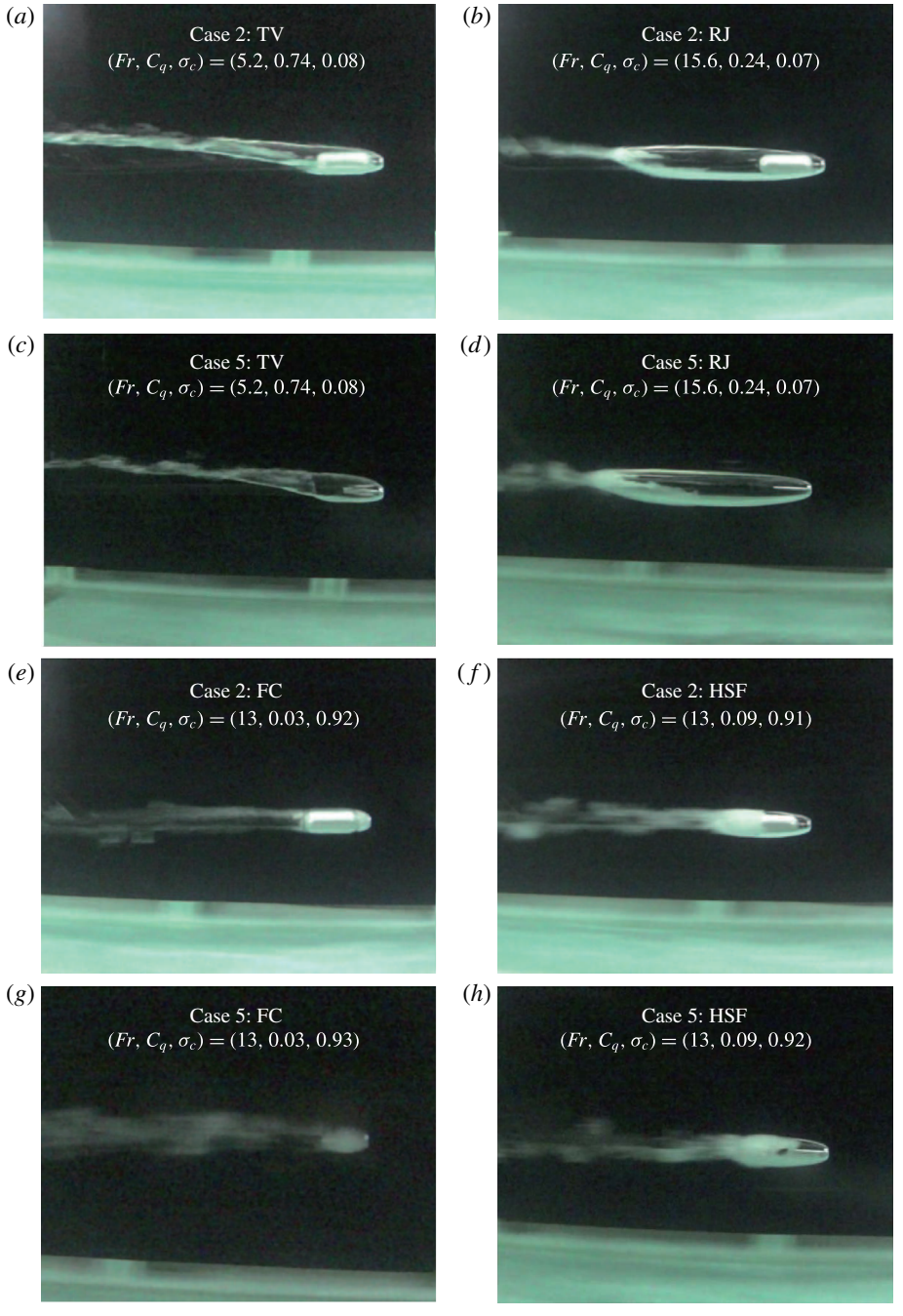

FIGURE 4. (Colour online) Comparison between cases 2 and 5 for the same set of (Fr, C_q, σ_c). A body exists for case 2 ($d^* = 0.5$, $B = 1.5\,\%$, $h^* = 0.5$) and no body exists for case 5 ($d^* = \infty$, $B = 1.5\,\%$, $h^* = 0.5$).

https://doi.org/10.1017/jfm.2018.638 Published online by Cambridge University Press

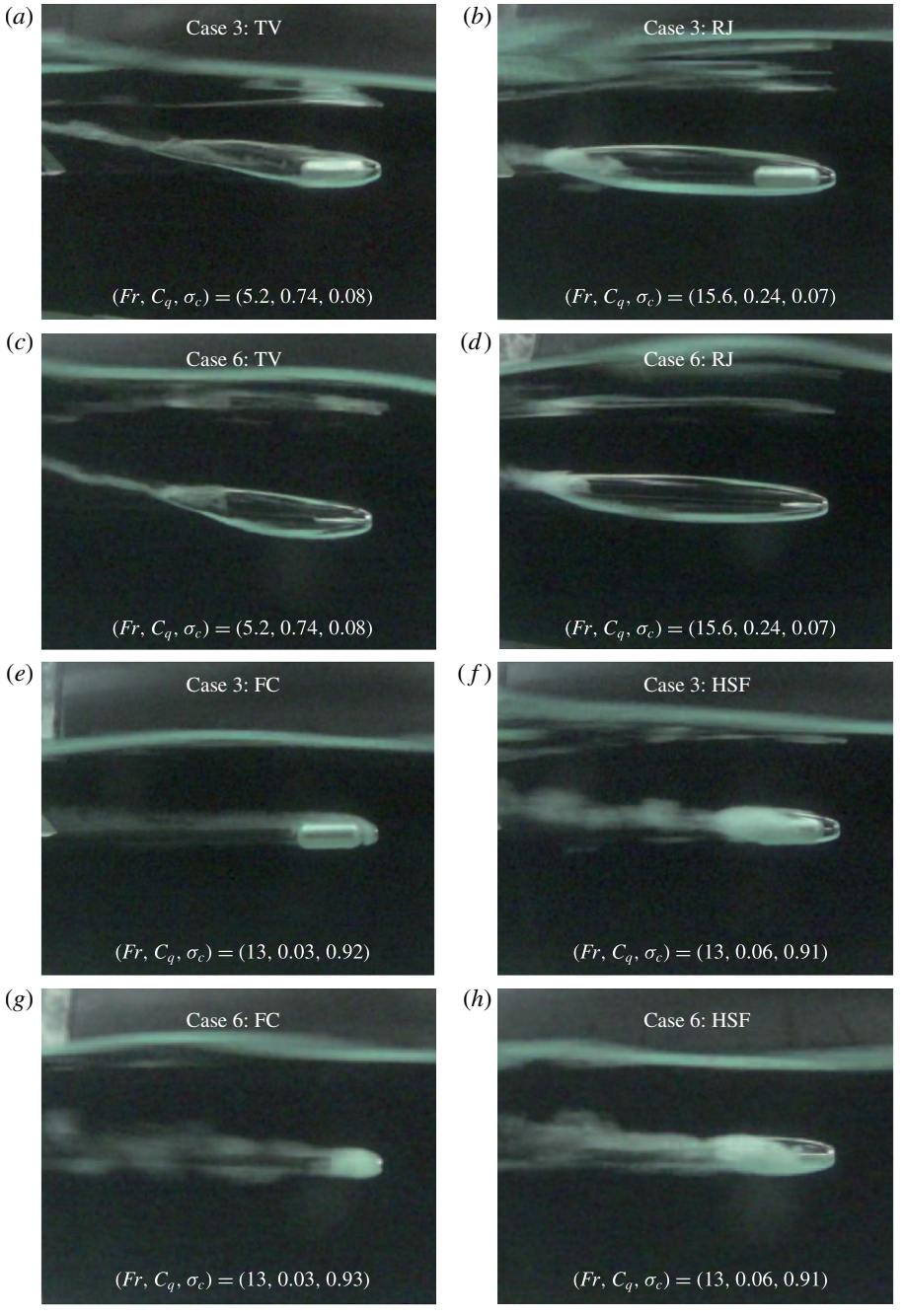

FIGURE 5. (Colour online) Comparison between cases 3 and 6 for the same set of (Fr, C_q, σ_c). A body exists for case 3 ($d^* = 0.5$, $B = 1.5\,\%$, $h^* = 0.17$) and no body exists for case 6 ($d^* = \infty$, $B = 1.5\,\%$, $h^* = 0.17$).

https://doi.org/10.1017/jfm.2018.638 Published online by Cambridge University Press

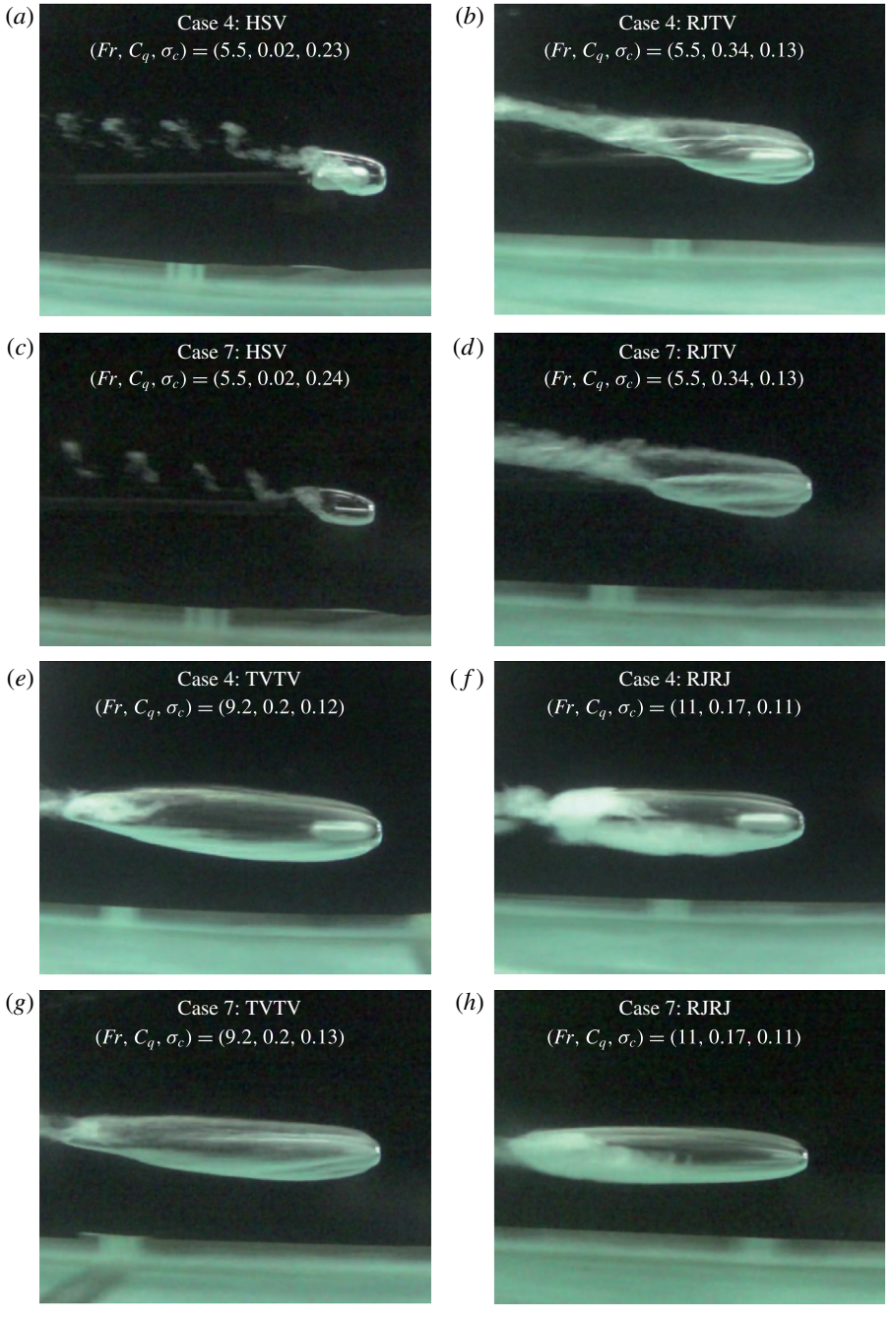

FIGURE 6. (Colour online) Comparison between cases 4 and 7 for the same set of (Fr, C_q, σ_c). A body exists for case 4 ($d^* = 0.5$, $B = 3\,\%$, $h^* = 0.5$) and no body exists for case 7 ($d^* = \infty$, $B = 3\,\%$, $h^* = 0.5$).

https://doi.org/10.1017/jfm.2018.638 Published online by Cambridge University Press

Case	Cavitator/body size	Blockage ratio	Submergence depth
	$d^* = d_c/d$ $(d = 0)$	$B = d_c/d_h$	$h^* = h_s/H$
5	$d^* = \infty$ (small cavitator)	$B = 1.5\,\%$	Fully submerged $h^* = 0.5$
6	$d^* = \infty$ (small cavitator)	$B = 1.5\,\%$	Shallowly submerged $h^* = 0.17$
7	$d^* = \infty$ (large cavitator)	$B = 3\,\%$	Fully submerged $h^* = 0.5$

TABLE 2. Three experimental conditions corresponding to cases 2, 3 and 4 in table 1 when a body does not exist $(d = 0)$ behind the cavitator; d_c is the diameter of the cavitator, H is the water depth, W is the channel width, d_h is the hydraulic diameter of the channel and h_s is the submergence depth.

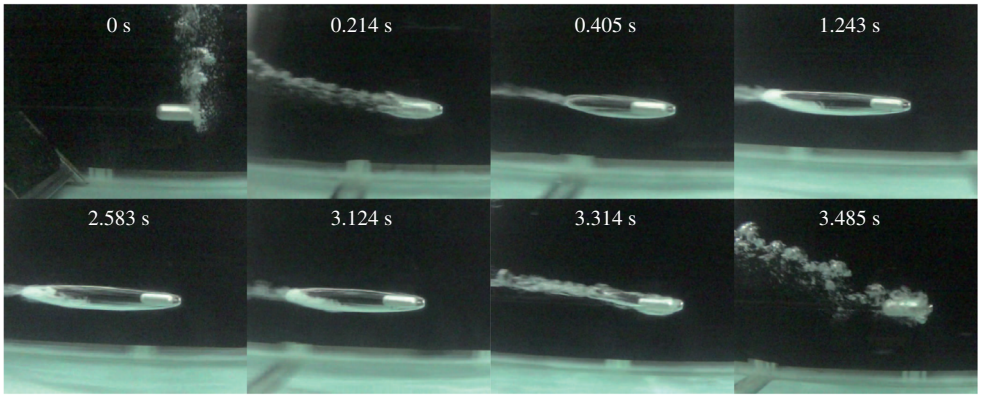

FIGURE 7. (Colour online) Whole process of the formation of a supercavity around a fully submerged moving body with a small blockage ratio ($Fr = 13.0$, $C_q = 0.44$, $\sigma_c = 0.06$). The accelerating phase is 1.243 s, the constant-speed phase is 1.88 s (1.243–3.124 s) and the decelerating phase is 0.36 s (3.124–3.485 s); one example of case 2 in table 1.

for the target steady-state speed of 5 m s^{-1} ($Fr = 13.0$) and the ventilation flow rate of 30 l min^{-1} ($C_q = 0.44$) with a resultant cavity pressure of 0.1 MPa ($\sigma_c = 0.06$). In this fully submerged case, due to the appreciable difference between the tank size and the body size, neither apparent wave motion on the free surface nor reflection effects from the side walls or bottom were observed during the motion of the underwater body. In this case, the accelerating phase is 1.243 s, the constant-speed phase is 1.88 s (1.243–3.124 s) and the decelerating phase is 0.36 s (3.124–3.485 s) (figure 7). At $t = 0$ s, a group of air bubbles at the body nose are shown which are supplied by the compressor. As the body starts to move, at $t = 0.214$ s, the cavity formation can be seen around the body with its air-bubble tail slightly upwards. At this stage, the cavity length is almost the same as the body length and the shape of the cavity is wrinkled and asymmetric in the transverse direction. From $t = 0.214$ to $t = 0.405$ s, the cavity length is increased and the shape of the cavity becomes smooth and more symmetric in the transverse direction. Thereafter until $t = 3.124$ s, the cavity finally becomes a supercavity which envelops the whole body and the shape of the cavity is a symmetric smooth-surface ellipsoid with a reentrant jet downstream. Thereafter until $t = 3.485$ s, the reverse images of the accelerating phase ($t = 0$ to $t = 1.243$ s) can be seen (the decelerating phase).

https://doi.org/10.1017/jfm.2018.638 Published online by Cambridge University Press

https://doi.org/10.1017/jfm.2018.638 Published online by Cambridge University Press

	Q (l min^{-1})																								
V (m s^{-1})	0	2	4	6	8	10	12	14	16	18	20	22	24	26	28	30	35	40	45	50	54	59	64	68	73
1	x	B	B	B	B	B	B	B	B	B	B	B	B	B	B	B	B	B	B	B	B	B	B	B	B
2	x	FC	FC	FC	FC	FC	FC	FC	FC	FC	FC	FC	FC	FC	FC	FC	FC	FC	FC	FC	FC	FC	FC	FC	FC
3	x	FC	FC	FC	FC	FC	FC	FC	FC	FC	FC	FC	FC	FC	FC	FC	FC	FC	FC	FC	FC	FC	FC	FC	FC
4	x	FC	FC	FC	FC	FC	FC	FC	FC	FC	FC	FC	FC	FC	FC	FC	FC	FC	FC	FC	FC	FC	FC	FC	FC
5	x	FC	FC	FC	FC	FC	FC	FC	FC	FC	FC	FC	FC	FC	FC	FC	FC	FC	FC	FC	FC	FC	FC	FC	FC
6	x	FC	FC	FC	FC	FC	FC	FC	FC	FC	FC	FC	FC	FC	FC	FC	FC	FC	FC	FC	FC	FC	FC	FC	FC
7	x	FC	FC	FC	FC	FC	FC	FC	FC	FC	FC	FC	FC	FC	FC	FC	FC	FC	FC	FC	FC	FC	FC	FC	FC

TABLE 3. Operational table for the steady-state phenomena around a fully submerged moving body without a cavitator (case 1 ($B = 0$, $h^* = 0.5$) in table 1) at various speeds (V: m s^{-1}) and ventilation flow rates (Q: l min^{-1}). x: no bubbles or cavities, B: bubbly flow, FC: foamy cavity.

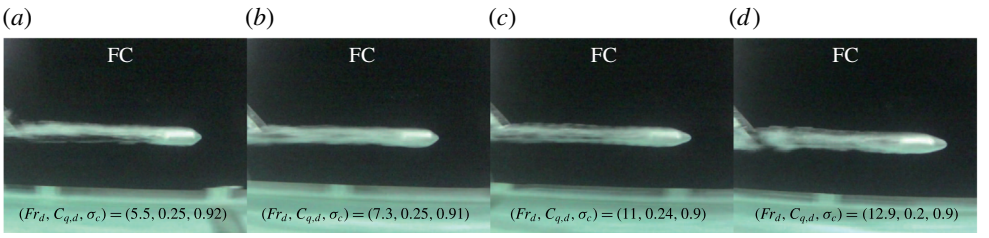

FIGURE 8. (Colour online) Side view observation of steady-state phenomena around a fully submerged moving body without a cavitator at various $Fr_d = V/(gd)^{1/2}$ ($Fr_d = 5.5$, 7.3, 11, 12.9) for a $C_{q,d} = 0.23 \pm 0.02$; case 1 ($B = 0$, $h^* = 0.5$) in table 1.

3.2. *Steady-state phenomena*

In this section, for each experimental case in table 1, the effects of the body speed (V) and the ventilation flow rate (Q) are investigated on the formation of a steady-state cavity with a resultant pressure (p_c) inside the cavity. Here, the body speed means the 'constant target speed'. The two dimensional quantities V and Q are operational parameters which can be controlled in the experiment. As a result, different types of steady-state cavities are formed around the body, and the resultant pressure (p_c) inside the cavity is measured. In other words, each different steady-state cavity formation depends on three dimensional parameters (V, Q, p_c), or, dimensionlessly speaking, (Fr, C_q, σ_c) for cases 2, 3, 4 and (Fr_d, $C_{q,d}$, σ_c) for case 1 (no cavitator). For each case, as in the previous section, the whole-process data are recorded using the carriage-attached cameras, from which steady-state phenomena are captured. For cases 2, 3 and 4, the ranges of (Fr, C_q, σ_c) are as follows; $Fr = 2.6$–18.2, $C_q = 0$–6, $\sigma_c = 0$–1 for cases 2 and 3, $Fr = 1.8$–12.9, $C_q = 0$–1.5, $\sigma_c = 0$–1 for case 4. The reason for the discrepancy of Fr and C_q between cases 2 and 3 and 4 originates mainly from the limited speed setting (1–7 m s^{-1}) due to the finite length of the wave tank and the limited volume flow rate provided by the compressor. Therefore, when it comes to comparison between cases 2 and 3 and 4, we choose the values of Fr and C_q closest to each other. For example, figures 11 and 12 (case 2) and figures 17 and 18 (case 3) are steady-state phenomena for $Fr = 5.2$, 7.8, 10.4, 13 with $C_q = 0.24 \pm 0.02$ and $C_q = 0.07$, 0.15, 0.22, 0.37 with $Fr = 5.2$. Correspondingly, figures 24 and 25 (case 4) are steady-state phenomena for $Fr = 5.5$, 7.3, 11, 12.9 with $C_q = 0.23 \pm 0.02$ and for $C_q = 0.05$, 0.15, 0.25, 0.34 with $Fr = 5.5$.

3.2.1. *Case1: no cavitator and fully submerged* ($B = 0$, $h^* = 0.5$)

Table 3 shows the operational table for the steady-state phenomena around a fully submerged moving body without a cavitator (case 1 in table 1) at various body speeds and ventilation flow rates. In the table, 'x' means no bubbles or cavities, 'B' means bubbly flow and 'FC' means a foamy cavity. In this case, no supercavitation is observed. Figure 8(*a–d*) shows steady-state phenomena at various Fr_d ($Fr_d = 5.5$, 7.3, 11, 12.9) for a constant $C_{q,d} = 0.23 \pm 0.02$. All are foamy cavities. The foamy cavity is not transparent. In all cases, the resultant σ_c is approximately 0.9. Figure 9(*a–d*) shows the steady-state phenomena at various $C_{q,d}$ ($C_{q,d} = 0.05$, 0.15, 0.25, 0.34) for a constant $Fr_d = 5.5$. As $C_{q,d}$ increases, the amount of a foamy cavity shed downstream increases, featuring more pointy air-filled bulge in front of the body nose. Corresponding to the operational table 3, for the physically meaningful dimensionless results, figure 10(*a–c*) shows the relationship between $C_{q,d}$ and Fr_d, between Fr_d

https://doi.org/10.1017/jfm.2018.638 Published online by Cambridge University Press

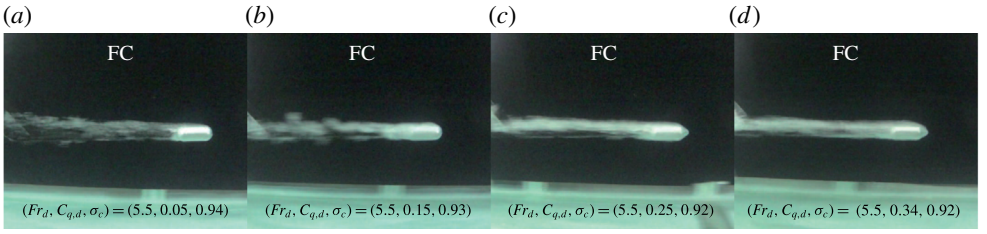

FIGURE 9. (Colour online) Side view observation of steady-state phenomena around a fully submerged moving body without a cavitator at various $C_{q,d}$ ($C_{q,d} = 0.05$, 0.15, 0.25, 0.34) for a constant Froude number ($Fr_d = 5.5$); case 1 ($B = 0$, $h^* = 0.5$) in table 1.

and σ_c and between σ_c and $C_{q,d}$ for the observed phenomena for case 1 ($B = 0$, $h^* = 0.5$) in table 1. Overall, a relatively high Fr_d favours a foamy cavity and a relatively low Fr_d favours bubbly flow. In addition, as can be seen from figure 10(*b*), for a constant $C_{q,d}$, the cavitation number σ_c slightly decreases as the Fr_d increases, which can be attributed to an increased rate of air entrainment at the cavity trailing edge. By comparing the results of the present no-cavitator case (case 1) with those of cases with cavitators (cases 2–4) in later sections, we will see that the cavitator is indispensable in the generation of supercavitation.

3.2.2. *Case 2: Small blockage and fully submerged* ($B = 1.5\,\%$, $h^* = 0.5$)

Table 4 shows the operational table for the steady-state phenomena around a fully submerged moving body with a small blockage ratio (case 2 in table 1) at various body speeds and ventilation flow rates. In the table, 'x' means no bubbles or cavities, 'B' bubbly flow, 'FC' a foamy cavity, 'TV' a twin-vortex supercavity, 'RJ' a reentrant-jet supercavity and 'HSF' a half-supercavity with a foamy cavity downstream. In case 2 ($B = 1.5\,\%$, $h^* = 0.5$), two supercavitation phenomena (TV, RJ) are clearly observed. For example, figure 11 shows side and top view steady-state phenomena at various Froude numbers ($Fr = 5.2$, 7.8, 10.4, 13) for a constant flow rate coefficient ($C_q = 0.24 \pm 0.02$). Compared to case 1, one can see the other side of the black tank wall through the cavity around the underwater body. At a low Fr (figure 11*a–c*), the supercavity is not fore–aft symmetric. This is twin-vortex supercavitation. Two vortex tails of the supercavity are directed upwards. For a high Fr (figure 11*d*), a rather smooth axisymmetric ellipsoidal supercavity can be seen and the supercavity has a tail with a reentrant-jet closure. Regardless of Fr-dependent differences, all the cases feature the smooth and axisymmetric nose of the cavity. The resultant σ_c are approximately 0.1 for the twin-vortex supercavities and the reentrant-jet supercavities. Compared to figure 11, figure 12 shows side and top view steady-state phenomena at various C_q ($C_q = 0.07$, 0.15, 0.22, 0.37) for a constant $Fr = 5.2$. Two different states are observed; a foamy cavity (figure 12*a*,*b*) and twin-vortex supercavities (figure 12*c*,*d*). The resultant σ_c values are 0.94 for the foamy cavity and 0.12 for the twin-vortex supercavities. Figures 11 and 12 correspond to some data for a constant $C_q = 0.24 \pm 0.02$ and for a constant $Fr = 5.2$, respectively, in figures 13–15. In figures 13–15, all the relevant dimensionless results are summarized in terms of the relationships between C_q and Fr, between Fr and σ_c and between σ_c and C_q, respectively. From figures 13–15, a relatively high Fr (>13) with $C_q = 0$–1 favours a reentrant-jet supercavity and a relatively low Fr (5–13) with $C_q = 0.1$–3 favours a twin-vortex supercavity. This trend may be compared with the most recent

https://doi.org/10.1017/jfm.2018.638 Published online by Cambridge University Press

https://doi.org/10.1017/jfm.2018.638 Published online by Cambridge University Press

	Q (l min^{-1})																							
V (m s^{-1})	0	2	4	6	8	10	12	14	16	18	20	22	24	26	28	30	35	40	45	50	54	59	64	68	73
1	x	B	B	B	B	B	B	B	B	B	B	B	B	B	B	B	B	B	B	B	B	B	B	B	B
2	x	FC	FC	TV	TV	TV	TV	TV	TV	TV	TV	TV	TV	TV	TV	TV	TV	TV	TV	TV	TV	TV	TV	TV	TV
3	x	FC	FC	TV	TV	TV	TV	TV	TV	TV	TV	TV	TV	TV	TV	TV	TV	TV	TV	TV	TV	TV	TV	TV	TV
4	x	FC	FC	TV	TV	TV	TV	TV	TV	TV	TV	TV	TV	TV	TV	TV	TV	TV	TV	TV	TV	TV	TV	TV	TV
5	x	FC	FC	HSF	RJ	RJ	RJ	RJ	RJ	RJ	RJ	RJ	RJ	RJ	RJ	RJ	RJ	RJ	RJ	RJ	RJ	RJ	RJ	RJ	RJ
6	x	FC	FC	HSF	RJ	RJ	RJ	RJ	RJ	RJ	RJ	RJ	RJ	RJ	RJ	RJ	RJ	RJ	RJ	RJ	RJ	RJ	RJ	RJ	RJ
7	x	FC	FC	HSF	RJ	RJ	RJ	RJ	RJ	RJ	RJ	RJ	RJ	RJ	RJ	RJ	RJ	RJ	RJ	RJ	RJ	RJ	RJ	RJ	RJ

TABLE 4. Operational table for the steady-state phenomena around a fully submerged moving body with a small blockage ratio (case 2 ($B = 1.5\,\%$, $h^* = 0.5$) in table 1) at various speeds (V: m s^{-1}) and ventilation flow rates (Q: l min^{-1}). x: no bubbles or cavities, B: bubbly flow, FC: foamy cavity, TV: twin-vortex supercavity, RJ: reentrant-jet supercavity, HSF: half-supercavity with foamy cavity downstream.

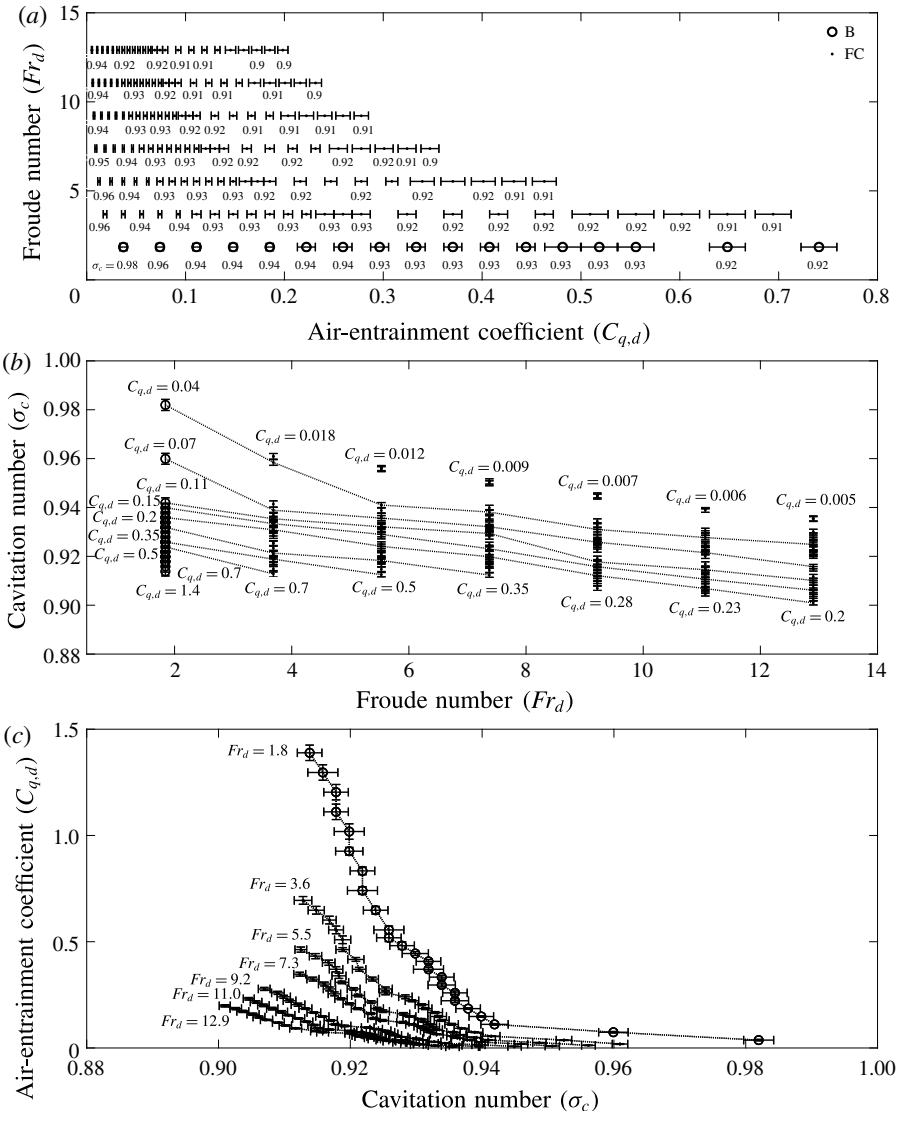

FIGURE 10. Experimental relationship among dimensionless parameters in case 1 ($B = 0$, $h^* = 0.5$) in table 1. (*a*) $C_{q,d}$ versus Fr_d, (*b*) Fr_d versus σ_c, (*c*) σ_c versus $C_{q,d}$.

experimental results in a closed water tunnel by Karn *et al.* (2016). With the same definitions of C_q and Fr as those of the present work, for the least blockage ratio $B = 5\,\%$ in their work, a reentrant-jet supercavity occurs when both C_q and Fr are relatively low ($C_q = 0.02$–0.04, $Fr = 10$–20), while a twin-vortex supercavity occurs when both C_q and Fr are relatively high ($C_q > 0.2$, $Fr > 10$–20). Karn *et al.* (2016) posit that the closure mechanism is mainly determined by the pressure difference across the gas–water interface at the cavity closure.

$$2\frac{p_{out} - p_{in}}{\rho V^2} = \widetilde{p}_{out} - \widetilde{p}_{in} = \Delta\widetilde{p}, \tag{3.4}$$

https://doi.org/10.1017/jfm.2018.638 Published online by Cambridge University Press

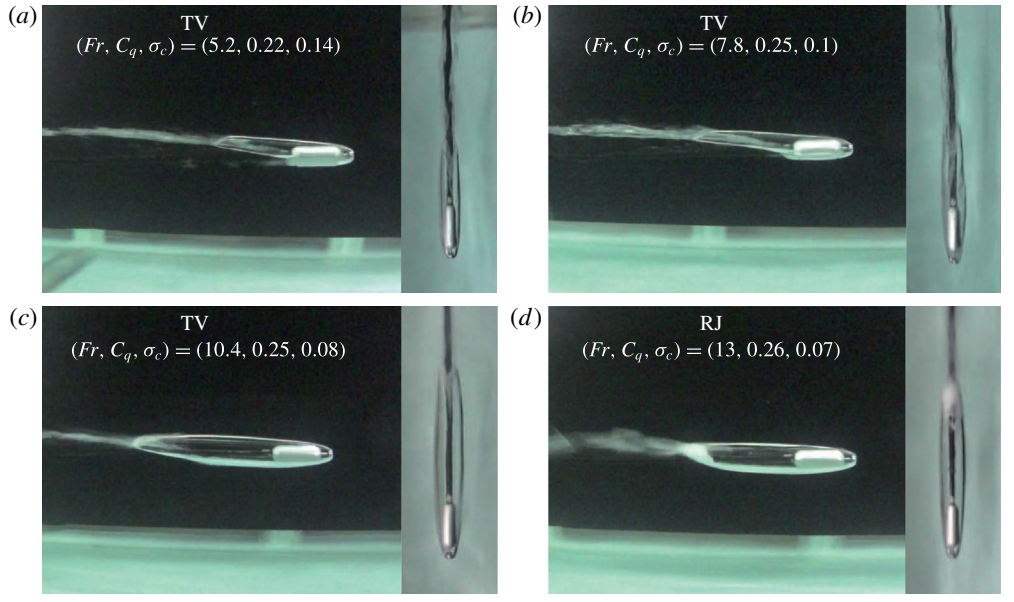

FIGURE 11. (Colour online) Side view and top view observations of steady-state phenomena around a fully submerged moving body with a small blockage ratio at various Froude numbers ($Fr = 5.2,\ 7.8,\ 10.4,\ 13$) for a constant flow rate coefficient ($C_q = 0.24 \pm 0.02$); case 2 ($B = 1.5\,\%,\ h^* = 0.5$) in table 1.

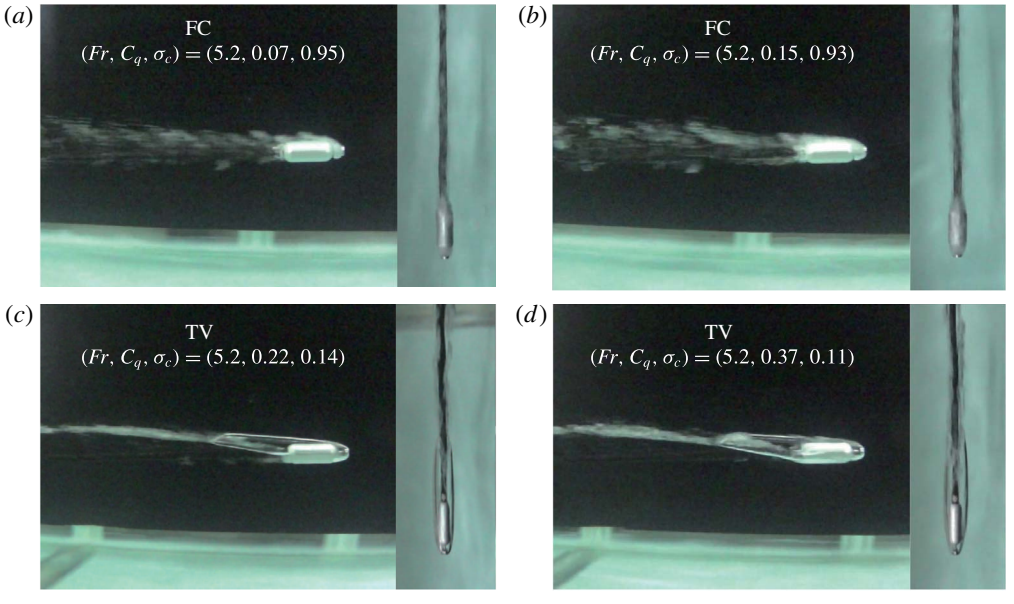

FIGURE 12. (Colour online) Side view and top view observations of steady-state phenomena around a fully submerged moving body with a small blockage ratio at various C_q ($C_q = 0.07,\ 0.15,\ 0.22,\ 0.37$) for a constant Froude number ($Fr = 5.2$); case 2 ($B = 1.5\,\%,\ h^* = 0.5$) in table 1.

https://doi.org/10.1017/jfm.2018.638 Published online by Cambridge University Press

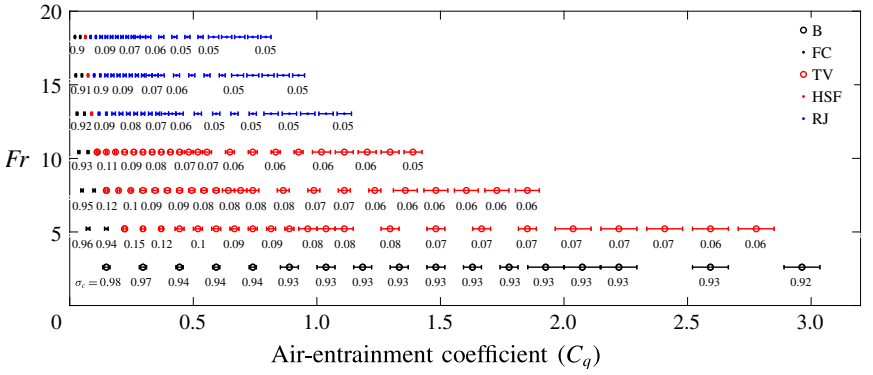

FIGURE 13. (Colour online) Air-entrainment coefficient (C_q) versus Froude number (Fr) for various steady states for case 2 ($B = 1.5\,\%$, $h^* = 0.5$) in table 1.

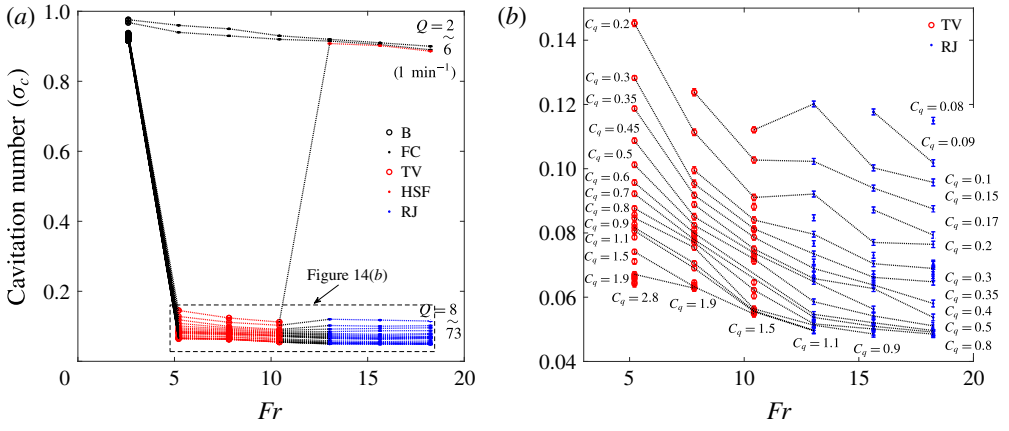

FIGURE 14. (Colour online) Froude number (Fr) versus cavitation number (σ_c) for case 2 ($B = 1.5\,\%$, $h^* = 0.5$) in table 1. (*a*) All states, (*b*) TV and RJ.

where, p_{in} and p_{out} are pressures inside and outside the cavity at the closure. For the reentrant-jet (RJ) supercavity, the $\Delta\widetilde{p}$ is dominated by the momentum of the reentrant water jet, while for a twin-vortex (TV) supercavity, such difference is much smaller, i.e. $\Delta\widetilde{p}_{RJ} \gg \Delta\widetilde{p}_{TV}$. Therefore, according to (3.4), for fixed B and Fr, high C_q implies an increase of cavity pressure, which results in higher $\widetilde{p}_{in}$. On the other hand, $\widetilde{p}_{out}$ is little dependent on C_q. Therefore, the resultant decrement in $\Delta\widetilde{p}$ leads to a twin-vortex supercavity. At a high Fr, however, the favoured formation of a twin-vortex supercavity cannot be readily explained using (3.4). In summary, in a closed environment ($B = 5\,\%$), high C_q and Fr favours a TV and low C_q and Fr favours an RJ. On the contrary, in a free-surface environment without any surface disturbance ($B = 1.5\,\%$), a high Fr favours an RJ and a low Fr favours a TV, which is also different from Campbell & Hilborne's (1958) work. Their work was carried out in a circular free-surface water channel (water depth: 0.46 m, channel width: 0.91 m, submergence depth: 0.22 m) with disk-type cavitators (diameter: 0.013 m, 0.019 m, 0.025 m, blockage ratio $B = 1.4\,\%$, $2.1\,\%$, $2.8\,\%$, $h^* = 0.47$) although they did not consider the effect of the closeness of the free surface on the formation of

https://doi.org/10.1017/jfm.2018.638 Published online by Cambridge University Press

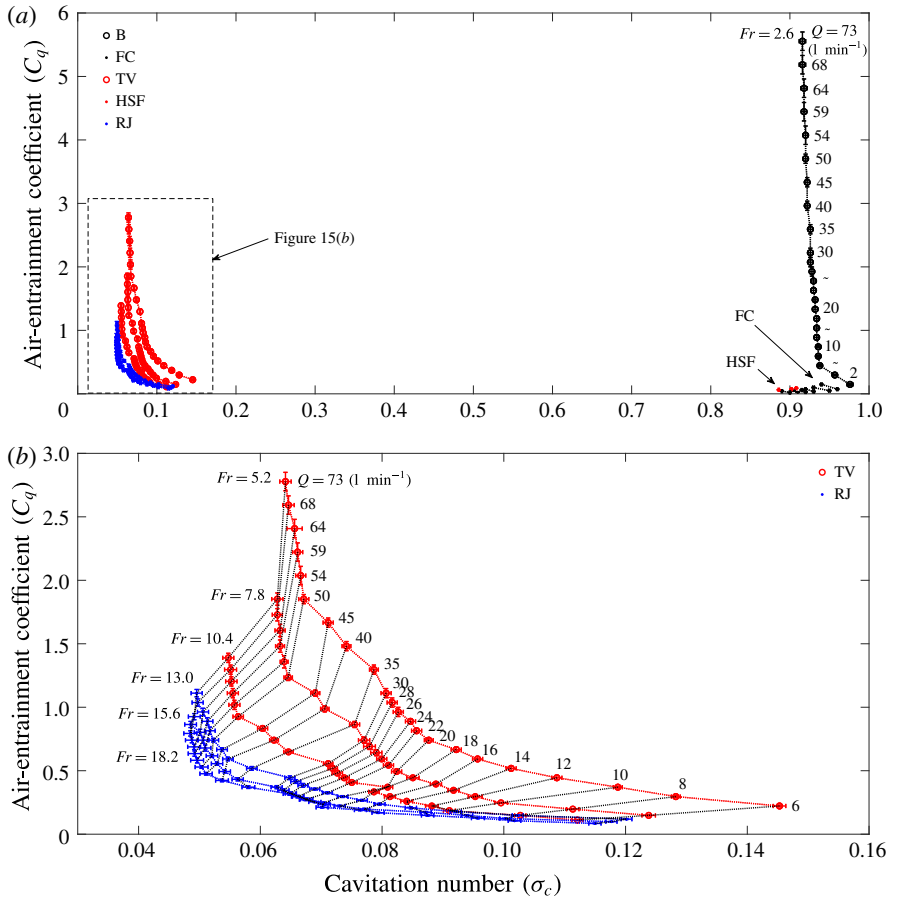

FIGURE 15. (Colour online) Cavitation number (σ_c) versus air-entrainment coefficient (C_q) for case 2 ($B = 1.5\,\%$, $h^* = 0.5$) in table 1. (*a*) All states, (*b*) TV and RJ.

the supercavity. Our case 2 ($B = 1.5\,\%$, $h^* = 0.5$) is similar to their case ($B = 1.4\,\%$, $h^* = 0.47$). They showed that an RJ supercavity occurs when $\sigma_c Fr > 1$ and a TV supercavity occurs when $\sigma_c Fr < 1$. This does not agree with our case 2. Figure 14(*a*,*b*) shows the relationship between Fr and σ_c for various C_q. In figure 14(*a*), where all states are shown, one can see that the resultant σ_c for the B, FC and HSF states are approximately 0.9, while the resultant σ_c values for supercavitation (RJ and TV) are around 0.1. The large jump in the figure represents the state change from TV to HSF. The air flow rate coefficient C_q is just sufficient to make a TV supercavity for low $Fr = 5.2$–10.4, but is not sufficient to make an RJ supercavity for high $Fr = 13$–18.2. Instead, the intermediate states HSF between TV and RJ are formed, which results in a high σ_c of around 0.9. Figure 15(*a*,*b*) shows the relationship between C_q and σ_c for various Fr, for all states and the supercavity states of the RJ and TV, respectively. For a given Fr, it is seen that a minimum cavitation number ($\sigma_{c,min}$) exists, regardless of the increase in the air flow rate (figure 15*b*). The values of $\sigma_{c,min} = 0.064$, 0.063, 0.055, 0.05, 0.049, 0.048 for $Fr = 5.2$, 7.8, 10.4, 13, 15.6, 18.2, respectively. The curves are L-shaped. On the horizontal branch of the L-shaped curve (where $\sigma_c > \sigma_{c,min}$), a small increase of Q (or C_q) causes a large increase of the cavity pressure (p_c) (or a large

https://doi.org/10.1017/jfm.2018.638 Published online by Cambridge University Press

decrease of σ_c) and the length, width and height of a supercavity or an increase of the cavity volume. This is due to the difficulty of the air escaping from the cavity. On the other hand, on the vertical branch of the L-shaped curve (where $\sigma_c \sim \sigma_{c,min}$), further increments to the air-entrainment rate are simply balanced by an increase in the rate of air evacuation through the cavity's trailing edge. At this point, the cavity pressure ceases to increase any further; the self-limiting behaviour establishes a minimum σ_c. All these can be confirmed from figure 16(*a*,*b*) where the normalized length (l/d_c), height (h/d_c) and width (w/d_c) of an RJ supercavity according to σ_c are shown for $Fr = 13$, 15.6 and 18.2. As shown in figure 16(*a*), for each Fr, the cavity length increases as σ_c decreases and becomes clustered near $\sigma_{c,min}$. Also, there is little difference for different $Fr = 13$, 15.6 and 18.2 for $0.045 < \sigma_c < 0.12$, in particular, there is a good collapse for $0.045 < \sigma_c < 0.055$ and a small spread in the data for $0.055 < \sigma_c < 0.12$. The empirical formula, neglecting small Fr-dependent spread, between the cavity length (l/d_c) and σ_c is as follows;

$$\frac{l}{d_c} = \frac{0.8661}{\sigma_c^{1.18}}. \tag{3.5}$$

For the cavity width and height, for each Fr, similar trends according to σ_c can be seen in figure 16(*b*). In addition, the cavity width is larger than the cavity height for each Fr. Unlike length (l/d_c) versus σ_c in figure 16(*a*), the Fr-dependence can be clearly seen in width (w/d_c) versus σ_c and height (h/d_c) versus σ_c in figure 16(*b*). As the Fr increases, the height and the width all increase, where the degree of the increment of the cavity height is relatively small compared to that of the cavity width. For $0.045 < \sigma_c < 0.07$, the height data collapse while the width data do not. The empirical formulas for the cavity width (w/d_c), height (h/d_c) and σ_c are as follows:

$$\frac{h}{d_c} = \begin{cases} \dfrac{1.3}{\sigma_c^{0.37}} & (Fr = 13) \\ \dfrac{1.35}{\sigma_c^{0.36}} & (Fr = 15.6) \\ \dfrac{1.52}{\sigma_c^{0.32}} & (Fr = 18.2), \end{cases} \tag{3.6}$$

$$\frac{w}{d_c} = \begin{cases} \dfrac{1.54}{\sigma_c^{0.35}} & (Fr = 13) \\ \dfrac{1.74}{\sigma_c^{0.32}} & (Fr = 15.6) \\ \dfrac{1.83}{\sigma_c^{0.31}} & (Fr = 18.2). \end{cases} \tag{3.7}$$

Also, in figure 16(*a*,*b*), we compare our results with existing analytical (Garabedian 1955) and semi-empirical works (Reichardt 1946; Waid 1957). With the assumption of steady, inviscid, irrotational, incompressible fluid flow, Garabedian (1955) presented the following asymptotic analytical formulas for the dimensionless length and height (width) of a natural axisymmetric supercavity around a disk-type cavitator in an unbounded fluid;

$$\frac{l}{d_c} = \frac{\sqrt{0.827(1+\sigma_c)}}{\sigma_c}\sqrt{\ln\frac{1}{\sigma_c}}, \tag{3.8}$$

https://doi.org/10.1017/jfm.2018.638 Published online by Cambridge University Press

$$\frac{h}{d_c} = \frac{w}{d_c} = \sqrt{\frac{0.827(1+\sigma_c)}{\sigma_c}}. \tag{3.9}$$

Reichardt (1946) suggested the following semi-empirical formulas for the dimensionless length and height (width) of a natural axisymmetric supercavity around an axisymmetric body with a disk-type cavitator;

$$\frac{l}{d_c} = \sqrt{\frac{0.827(1+\sigma_c)}{\sigma_c - 0.132\sigma_c^{1.142857}}}\,\frac{\sigma_c + 0.008}{\sigma_c(0.066 + 1.7\sigma_c)}, \tag{3.10}$$

$$\frac{h}{d_c} = \frac{w}{d_c} = \sqrt{\frac{0.827(1+\sigma_c)}{\sigma_c - 0.132\sigma_c^{1.142857}}}. \tag{3.11}$$

Waid (1957) suggested the following semi-empirical formulas for the dimensionless length and height (width) of a ventilated supercavity around an axisymmetric body with a disk-type cavitator in a free-surface water tunnel, where the model was placed in the centre of the width and 12 inches above the bottom of the 20-by-20-inch test section. In our notation, the submergence depth is $h^* = 8/20 = 0.4$.

$$\frac{l}{d_c} = \frac{1.08}{\sigma_c^{1.118}}, \tag{3.12}$$

$$\frac{h}{d_c} = \frac{w}{d_c} = \frac{0.534}{\sigma_c^{0.568}} + 1. \tag{3.13}$$

As shown in figure 16(*a*,*b*), the length and the height of a supercavity with a reentrant jet in the present work, for the most part, agree with those from the above three existing works (3.8)–(3.13). These three works agree with each other, showing a better agreement as σ_c increases, even if the physical settings from which these equations are derived are all different. In particular, Waid's (1957) work is closest to the present experiment although the dimensionless submergence depth is different; $h^* = 0.5$ for our case 2 (and $h^* = 0.17$ for our case 3 in the next subsection § 3.2.3). The cavity length data are a little below Waid's equation (3.12) and show a good agreement for $0.045 < \sigma_c < 0.055$. The cavity height data are spread but overlaid on (3.9), (3.11) and (3.13), showing good agreement for $0.045 < \sigma_c < 0.055$. Finally, all the cavity width data are well above (3.9), (3.11) and (3.13).

3.2.3. *Case 3: small blockage and shallowly submerged* ($B = 1.5\,\%$, $h^* = 0.17$)

To see the effect of the closeness of a body to the free surface on the supercavitation, we performed experiments for the shallowly submerged case with the same blockage ratio as case 2 which is fully submerged. Table 5 shows the operational table for the steady-state phenomena around a shallowly submerged moving body with a small blockage ratio (case 3 in table 1) at various body speeds and ventilation flow rates. It can be seen that there is little difference between table 4 (case 2) and table 5 (case 3) in terms of the categorization of steady-state phenomena. For example, the overall steady-state phenomena (figures 17 and 18) are similar to those in case 2 (figures 11 and 12) for the same set of (Fr, C_q). There are, however, differences in the detailed shapes of the cavity and the free surface. In case 3, the cavity shapes are not bottom–top symmetric and, also, the nearby free surface shows small-amplitude long waves due to the apparent shape of the supercavity around the moving body.

https://doi.org/10.1017/jfm.2018.638 Published online by Cambridge University Press

https://doi.org/10.1017/jfm.2018.638 Published online by Cambridge University Press

	Q (l min^{-1})																								
V (m s^{-1})	0	2	4	6	8	10	12	14	16	18	20	22	24	26	28	30	35	40	45	50	54	59	64	68	73
1	x	B	B	B	B	B	B	B	B	B	B	B	B	B	B	B	B	B	B	B	B	B	B	B	B
2	x	FC	TV	TV	TV	TV	TV	TV	TV	TV	TV	TV	TV	TV	TV	TV	TV	TV	TV	TV	TV	TV	TV	TV	TV
3	x	FC	TV	TV	TV	TV	TV	TV	TV	TV	TV	TV	TV	TV	TV	TV	TV	TV	TV	TV	TV	TV	TV	TV	TV
4	x	FC	TV	TV	TV	TV	TV	TV	TV	TV	TV	TV	TV	TV	TV	TV	TV	TV	TV	TV	TV	TV	TV	TV	TV
5	x	FC	HSF	RJ	RJ	RJ	RJ	RJ	RJ	RJ	RJ	RJ	RJ	RJ	RJ	RJ	RJ	RJ	RJ	RJ	RJ	RJ	RJ	RJ	RJ
6	x	FC	HSF	RJ	RJ	RJ	RJ	RJ	RJ	RJ	RJ	RJ	RJ	RJ	RJ	RJ	RJ	RJ	RJ	RJ	RJ	RJ	RJ	RJ	RJ
7	x	FC	HSF	RJ	RJ	RJ	RJ	RJ	RJ	RJ	RJ	RJ	RJ	RJ	RJ	RJ	RJ	RJ	RJ	RJ	RJ	RJ	RJ	RJ	RJ

TABLE 5. Operational table for the steady-state phenomena around a shallowly submerged moving body with a small blockage ratio (case 3 ($B = 1.5\,\%$, $h^* = 0.17$) in table 1) at various speeds (V: m s^{-1}) and ventilation flow rates (Q: l min^{-1}). x: no bubbles or cavities, B: bubbly flow, FC: foamy cavity, TV: twin-vortex supercavity, RJ: reentrant-jet supercavity, HSF: half-supercavity with foamy cavity downstream.

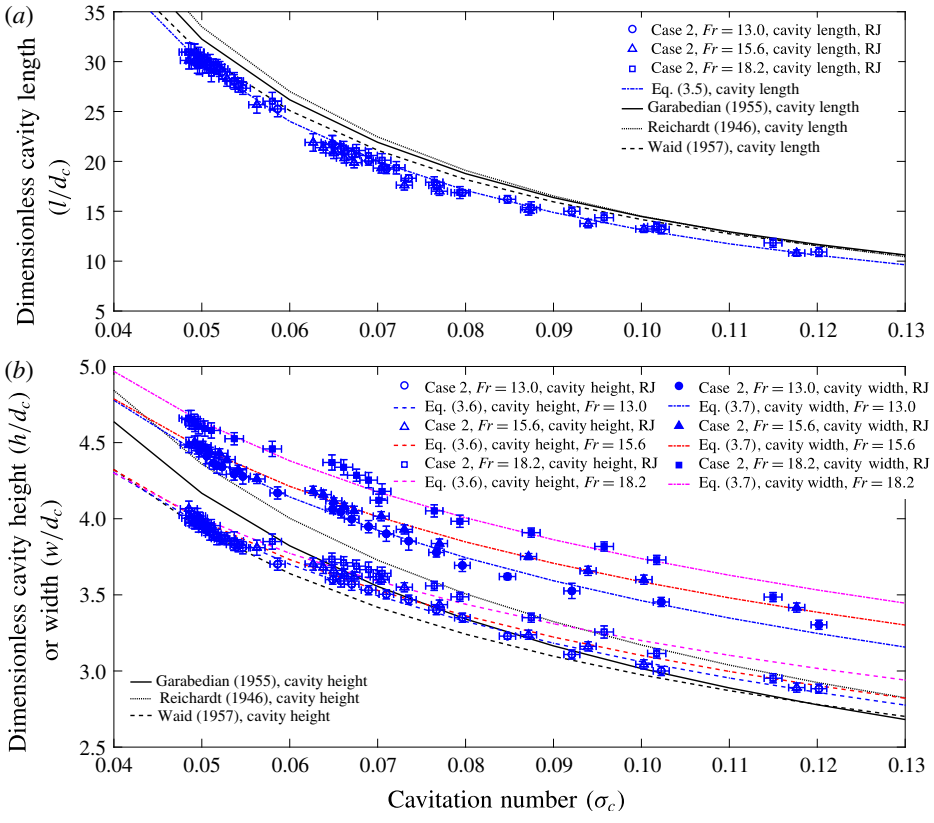

FIGURE 16. (Colour online) Normalized length (l/d_c), height (h/d_c) and width (w/d_c) of the reentrant-jet supercavity according to σ_c, where d_c is the diameter of the cavitator. (*a*) Normalized length, (*b*) normalized height and width; case 2 ($B = 1.5\,\%$, $h^* = 0.5$) in table 1.

The relationships among Fr, σ_c and C_q in case 3 (figures 19–21) are almost the same as those in case 2 (figures 13–15). In figures 19–21, all the relevant dimensionless results, including exemplary cases in figures 17 and 18, are summarized in terms of the relationships between C_q and Fr, between Fr and σ_c and between σ_c and C_q, respectively. In figure 19, as in case 2, a relatively high Fr (>13) with $C_q = 0$–1 favours a reentrant-jet supercavity and a relatively low Fr (5–13) with $C_q = 0.1$–3 favours a twin-vortex supercavity. Figure 20(*a*,*b*) shows the relationship between Fr and σ_c for various C_q. In figure 20(*a*) where all states are shown, one can see that the resultant σ_c for the B, FC and HSF states are approximately 0.9 while the resultant σ_c for supercavitation (RJ and TV) are approximately 0.1. The large jump in the figure represents a state change from a TV to a HSF. The air flow rate coefficient C_q is just sufficient to make a TV supercavity for low $Fr = 5.2$–10.4, but is not sufficient to make an RJ supercavity for high $Fr = 13$–18.2. Instead, the intermediate state HSF between a TV and RJ are formed, which results in a high σ_c around 0.9. Figure 21(*a*,*b*) shows the relationship between C_q and σ_c for various Fr, for all states and the supercavity states of RJ and TV, respectively. For a given Fr, it is seen that a minimum cavitation number ($\sigma_{c,min}$) exists, regardless of an increase in the air flow rate (figure 21*b*). The values are $\sigma_{c,min} = 0.063$, 0.061, 0.053, 0.048, 0.047, 0.046 for

https://doi.org/10.1017/jfm.2018.638 Published online by Cambridge University Press

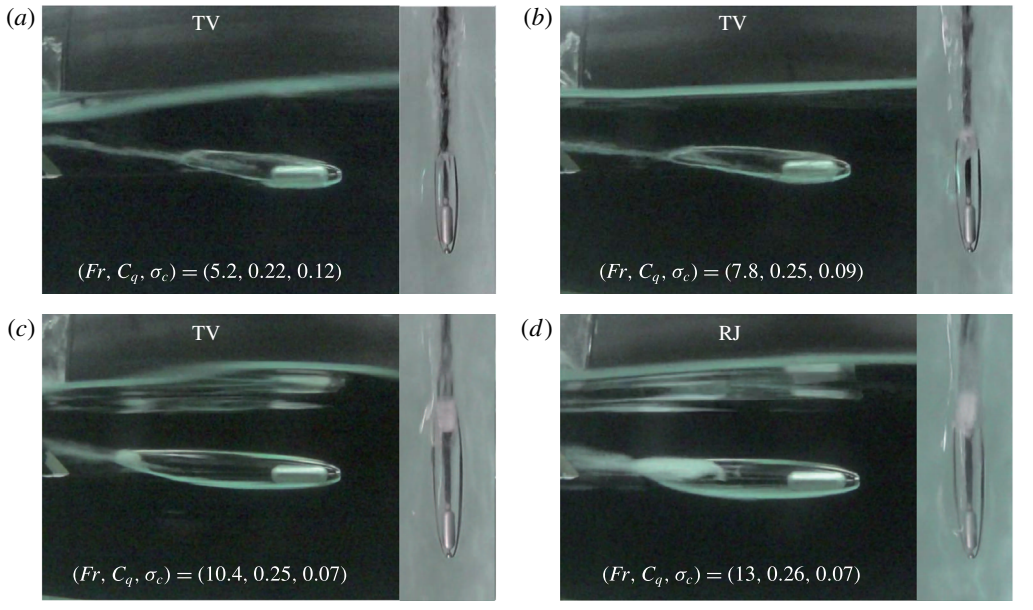

FIGURE 17. (Colour online) Side view and top view observations of steady-state phenomena around a shallowly submerged moving body with a small blockage ratio at various Froude numbers ($Fr = 5.2,\ 7.8,\ 10.4,\ 13$) for a constant flow rate coefficient ($C_q = 0.24 \pm 0.02$); case 3 ($B = 1.5\,\%,\ h^* = 0.17$) in table 1.

$Fr = 5.2,\ 7.8,\ 10.4,\ 13,\ 15.6,\ 18.2$, respectively. As shown in figure 22(*a*), for each Fr, the cavity length increases as σ_c decreases and becomes clustered near $\sigma_{c,min}$. Also, there is little difference for different $Fr = 13$, 15.6 and 18.2 for $0.045 < \sigma_c < 0.12$, in particular, a good collapse for $0.045 < \sigma_c < 0.055$ and a small spread in the data for $0.055 < \sigma_c < 0.12$. Overall, the length data in case 3 ($h^* = 0.17$) are smaller than those in case 2 ($h^* = 0.5$) for the same σ_c. The proportional relationship between h^* and l/d_c (or h_s and l) can be explained by reference to figure 23(*a*,*b*). Figure 23(*a*) represents an RJ supercavity and the nearby free surface and figure 23(*b*) represents a streamline between the upper surface of an RJ supercavity and the free surface above the RJ supercavity. By applying Bernoulli's theorem across the streamline in figure 23(*a*), one obtains the following equation:

$$\frac{p_{atm} - p_c}{h_s} \approx \rho \frac{V^2}{R}. \tag{3.14}$$

On the other hand, from figure 23(*b*), the radius of curvature R of the streamline and the cavity length l are geometrically related to each other as follows:

$$l \approx R(2\theta). \tag{3.15}$$

Then, from (3.14) and (3.15),

$$\frac{p_{atm} - p_c}{h_s} \approx \rho \frac{2\theta V^2}{l}. \tag{3.16}$$

https://doi.org/10.1017/jfm.2018.638 Published online by Cambridge University Press

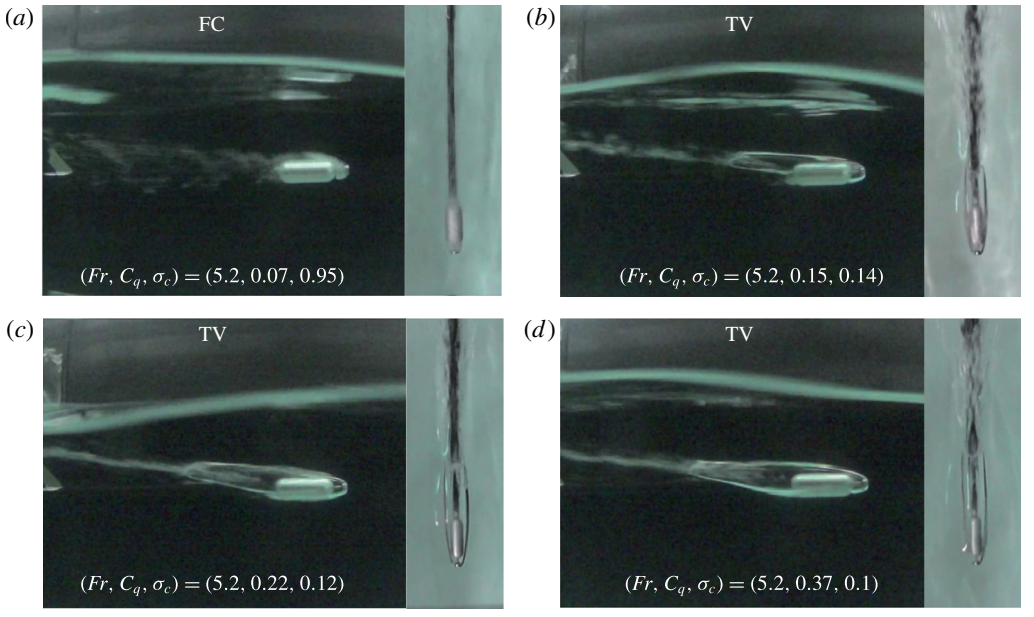

FIGURE 18. (Colour online) Side view and top view observations of steady-state phenomena around a shallowly submerged moving body with a small blockage ratio at various C_q ($C_q = 0.07,\ 0.15,\ 0.22,\ 0.37$) for a constant Froude number ($Fr = 5.2$); case 3 ($B = 1.5\,\%,\ h^* = 0.17$) in table 1.

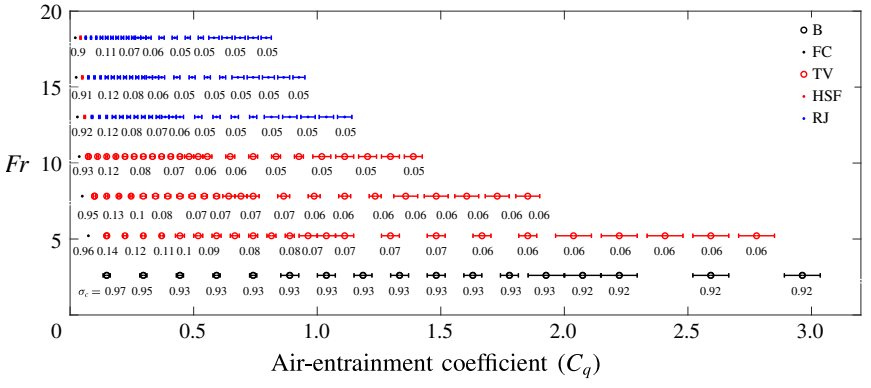

FIGURE 19. (Colour online) Air-entrainment coefficient (C_q) versus Froude number (Fr) for various steady states for case 3 ($B = 1.5\,\%,\ h^* = 0.17$) in table 1.

By rearranging (3.16) as follows,

$$l \approx \frac{4\theta h_s}{2(p_{atm} - p_c)/\rho V^2} = \frac{4\theta h_s}{\sigma_c}. \tag{3.17}$$

Thus, equation (3.17) explains the proportional relationship between h_s and l. In other words, for the same blockage ratio, the shallowly submerged case 3 results in a smaller cavity length compared to the fully submerged case 2. For the cavity width and height, for each Fr, similar trends to the cavity length according to σ_c can be

https://doi.org/10.1017/jfm.2018.638 Published online by Cambridge University Press

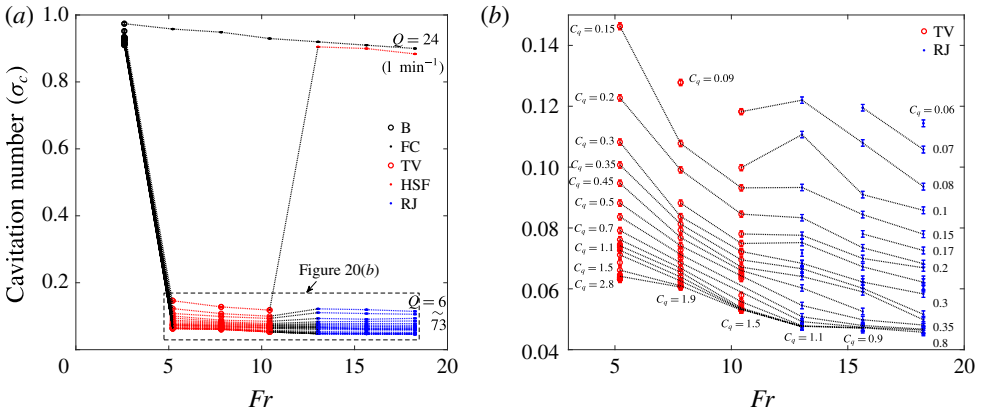

FIGURE 20. (Colour online) Froude number (Fr) versus cavitation number (σ_c) for case 3 ($B = 1.5\,\%$, $h^* = 0.17$) in table 1. (*a*) All states, (*b*) TV and RJ.

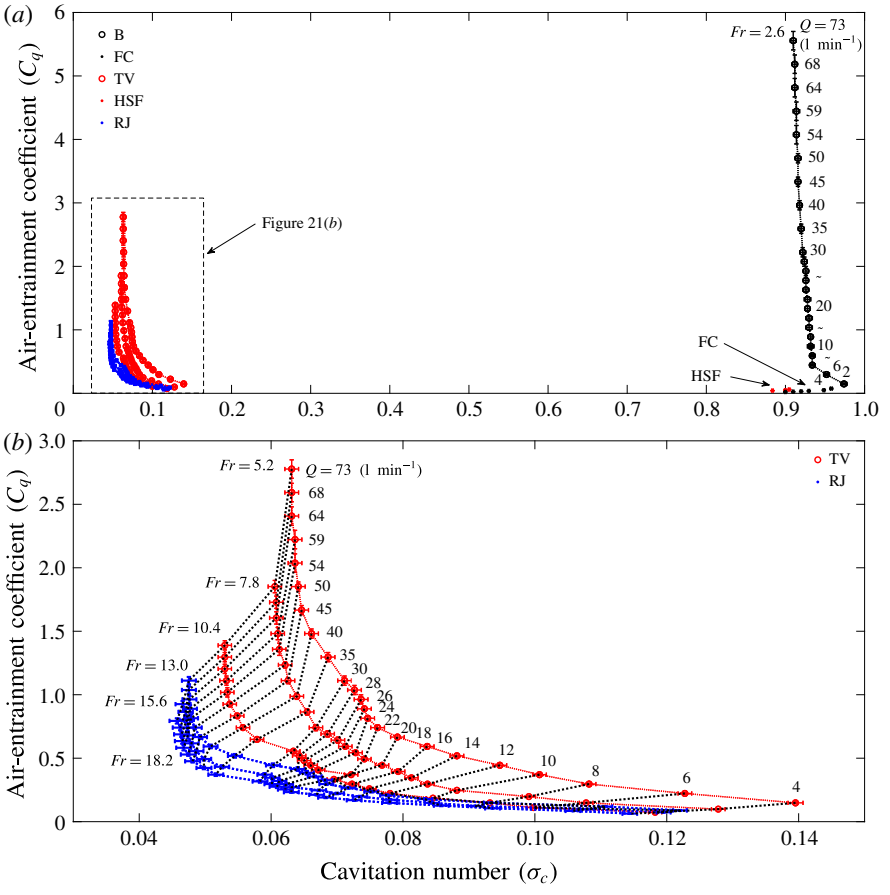

FIGURE 21. (Colour online) Cavitation number (σ_c) versus air-entrainment coefficient (C_q) for case 3 ($B = 1.5\,\%$, $h^* = 0.17$) in table 1. (*a*) All states, (*b*) TV and RJ.

https://doi.org/10.1017/jfm.2018.638 Published online by Cambridge University Press

seen in figure 22(*b*). In addition, the cavity width is larger than the cavity height for each *Fr*. As with (l/d_c) versus σ_c in figure 22(*a*), a very weak *Fr*-dependence can be seen in width (w/d_c) versus σ_c and height (h/d_c) versus σ_c in figure 22(*b*). In other words, the height and width data collapse regardless of the *Fr*, in particular, a better collapse for $0.045 < \sigma_c < 0.08$. Overall, compared to case 2, the height and width data in case 3 collapse better and such that the height data for $Fr = 13$, 15.6 approach those for $Fr = 18.2$. In case 3, by making a long wave above the supercavity, the free surface plays the role of limiting the growth of the width and height of a supercavity, thus annihilating the effect of the *Fr*. The empirical formulas for the cavity length (l/d_c), width (w/d_c) and height (h/d_c) are as follows

$$\frac{l}{d_c} = \frac{0.9513}{\sigma_c^{1.14}}, \tag{3.18}$$

$$\frac{h}{d_c} = \frac{1.4056}{\sigma_c^{0.36}}, \tag{3.19}$$

$$\frac{w}{d_c} = \frac{1.4984}{\sigma_c^{0.38}}. \tag{3.20}$$

3.2.4. *Case 4: Large blockage and fully submerged* ($B = 3\,\%$, $h^* = 0.5$)

In case 4 ($B = 3\,\%$, $h^* = 0.5$), where the blockage ratio is twice that of case 2 and the submergence depth of the body is the same as that of case 2 ($B = 1.5\,\%$, $h^* = 0.5$), the overall flow phenomena are observed to be quite different from case 2, which can be seen from tables 4 and 6 by comparison. In table 6, 'x' means no bubbles or cavities, 'B' bubbles, 'FC' a foamy cavity, 'TV' a twin-vortex supercavity, 'RJ' a reentrant-jet supercavity, 'HSV' a half-supercavity with a ring-type vortex shedding downstream, 'RJTV' a double-layer supercavity with a reentrant jet inside and twin vortices outside (figure 25*d*), 'TVTV' a double-layer supercavity with twin vortices inside and twin vortices outside (figure 24*b*) and 'RJRJ' a double-layer supercavity with a reentrant jet inside and a reentrant jet outside (figure 24*c*,*d*). Double-layer supercavities (RJTV, TVTV, RJRJ) in case 4 are not observed in either cases 2 or 3, and also were not observed in Campbell & Hilborne's (1958) work for similar conditions ($B = 2.8\,\%$, $h^* = 0.47$). In figure 26, for a better understanding of the flow structures, photo-based illustrations for the RJTV, TVTV and RJRJ supercavities are drawn, along with their real photos. The outlines of the inner and outer layers are most clearly seen for RJTV supercavities and are less obvious, but discernible, in the upper part of the cavities for the TVTV and RJRJ supercavities. Both the inner and the outer layers are composed of air, and, between the two, there exists a foamy interface. The glassy regions of double-layer supercavities are less transparent than those of single-layer supercavities. In addition, apparently, double-layer supercavities have more foamy regions inside the cavities than single-layer supercavities. In figures 27–29, all the relevant dimensionless results, including exemplary cases in figures 24 and 25, are summarized in terms of the relationships between C_q and *Fr*, between *Fr* and σ_c and between σ_c and C_q, respectively. Figures 24 and 25 correspond to representative data for a constant flow rate $C_q = 0.23 \pm 0.02$ and for a constant Froude number $Fr = 5.5$, respectively, in figures 27–29. In figure 27, for $Fr = 1.8$, all states (C_q: 0.03–0.74) are bubbly. For higher *Fr* values, we successively observe different steady-state phenomena as C_q increases at each *Fr*. For $Fr = 3.6$, HSV (C_q: 0.02–0.055)–TV (C_q: 0.07–0.46)–RJTV (C_q: 0.5–0.7). For $Fr = 5.5$,

https://doi.org/10.1017/jfm.2018.638 Published online by Cambridge University Press

https://doi.org/10.1017/jfm.2018.638 Published online by Cambridge University Press

	Q (l min^{-1})																								
V (m s^{-1})	0	2	4	6	8	10	12	14	16	18	20	22	24	26	28	30	35	40	45	50	54	59	64	68	73
1	x	B	B	B	B	B	B	B	B	B	B	B	B	B	B	B	B	B	B	B	B	B	B	B	B
2	x	HSV	HSV	HSV	TV	TV	TV	TV	TV	TV	TV	TV	TV	TV	TV	TV	TV	TV	TV	TV	RJTV	RJTV	RJTV	RJTV	RJTV
3	x	FC	HSV	HSV	HSV	TV	TV	TV	TV	TV	TV	TV	TV	TV	TV	TV	TV	TV	TV	TV	RJTV	RJTV	RJTV	RJTV	RJTV
4	x	FC	FC	FC	FC	FC	FC	FC	FC	FC	FC	FC	FC	FC	FC	FC	TV	TV	TV	TV	TVTV	TVTV	TVTV	TVTV	TVTV
5	x	FC	FC	FC	FC	FC	FC	FC	FC	FC	FC	FC	FC	FC	FC	FC	FC	FC	FC	FC	TVTV	TVTV	TVTV	TVTV	TVTV
6	x	FC	FC	FC	FC	FC	FC	FC	FC	FC	FC	FC	FC	FC	FC	FC	FC	FC	FC	FC	RJRJ	RJRJ	RJRJ	RJRJ	RJRJ
7	x	FC	FC	FC	FC	FC	FC	FC	FC	FC	FC	FC	FC	FC	FC	FC	FC	FC	FC	FC	RJRJ	RJRJ	RJRJ	RJRJ	RJRJ

TABLE 6. Operational table for the steady-state phenomena around a fully submerged moving body with a large blockage ratio (case 4 ($B = 3\,\%$, $h^* = 0.5$) in table 1) at various speeds (V: m s^{-1}) and ventilation flow rates (Q: l min^{-1}). x: no bubbles or cavities, B: bubbly flow, FC: foamy cavity, TV: twin-vortex supercavity, RJ: reentrant-jet supercavity, HSV: half-supercavity with ring-type vortex shedding downstream, RJTV: double-layer supercavity with a reentrant-jet inside and twin vortices outside, TVTV: double-layer supercavity with twin vortices inside and twin vortices outside, RJRJ: double-layer supercavity a reentrant-jet inside and a reentrant-jet outside.

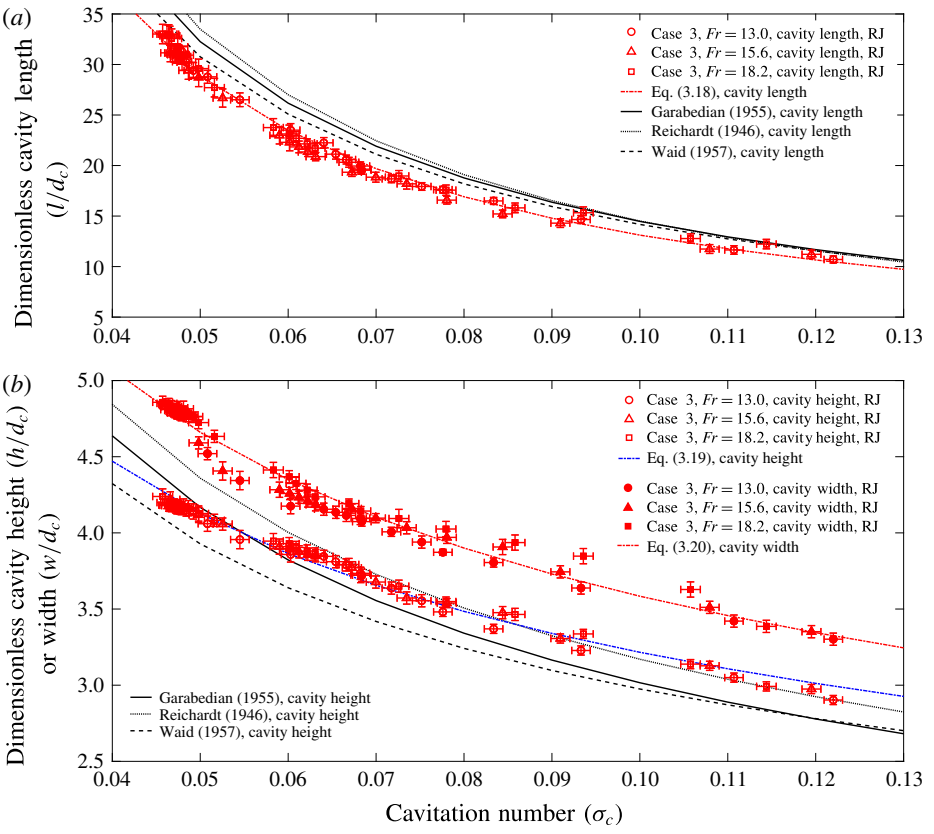

FIGURE 22. (Colour online) Normalized length (l/d_c), height (h/d_c) and width (w/d_c) of the reentrant-jet supercavity according to σ_c, where d_c is the diameter of the cavitator. (*a*) Normalized length, (*b*) normalized height and width; case 3 ($B = 1.5\,\%$, $h^* = 0.17$) in table 1.

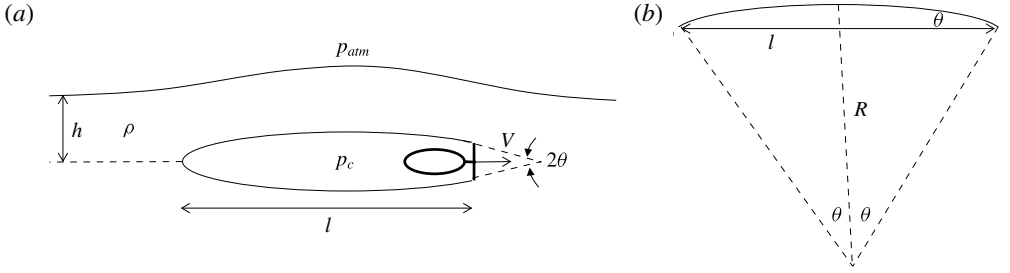

FIGURE 23. Schematics for an RJ supercavity in a fluid with a free surface. (*a*) RJ supercavity and the nearby free surface, (*b*) a streamline between the upper surface of the RJ supercavity and the free surface above the RJ supercavity.

FC (C_q: 0.01)–HSV (C_q: 0.02–0.05)–TV (C_q: 0.06–0.31)–RJTV (C_q: 0.34–0.46). For $Fr = 7.3$, FC (C_q: 0.01–0.14)–TV (C_q: 0.16–0.23)–TVTV (C_q: 0.25–0.35). For $Fr = 9.2$, FC (C_q: 0.007–0.18)–TVTV (C_q: 0.2–0.28). For $Fr = 11$, FC (C_q: 0.006–0.15)–RJRJ (C_q: 0.17–0.23). For $Fr = 12.9$, FC (C_q: 0.005–0.13)–RJRJ (C_q: 0.14–0.2).

https://doi.org/10.1017/jfm.2018.638 Published online by Cambridge University Press

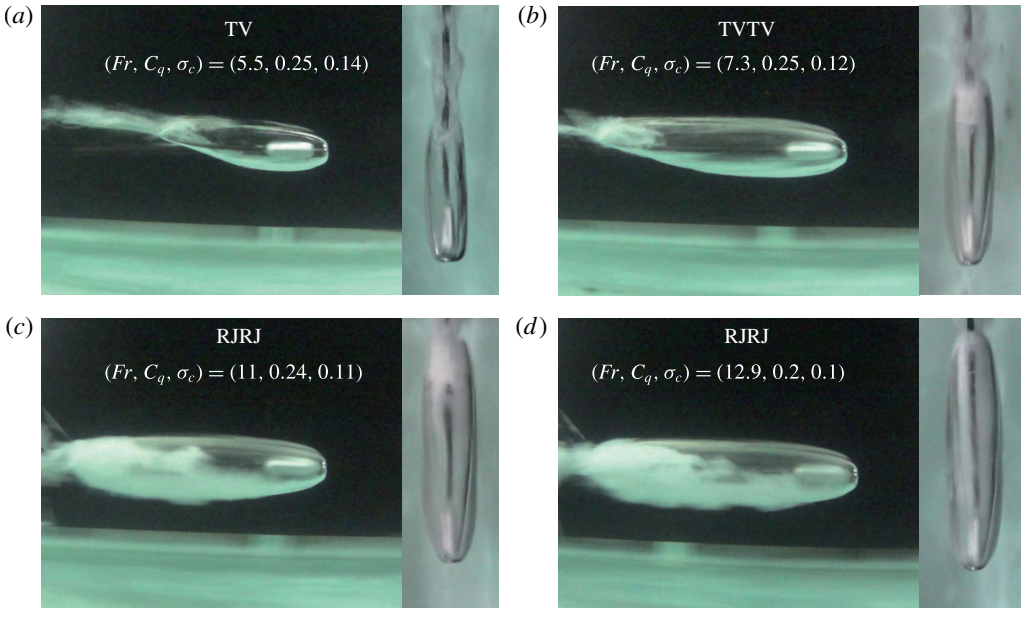

FIGURE 24. (Colour online) Side view and top view observations of steady-state phenomena around a fully submerged moving body with a large blockage ratio at various Froude numbers ($Fr = 5.5$, 7.3, 11, 12.9) for a constant flow rate coefficient ($C_q = 0.23 \pm 0.02$); case 4 ($B = 3\,\%$, $h^* = 0.5$) in table 1.

Figure 28(*a*,*b*) shows the relationship between Fr and σ_c for various C_q. In figure 28(*a*) where all states are shown, one can see that the resultant σ_c for the non-supercavitating states (B, FC) are approximately 0.9 while the resultant σ_c for supercavitation (TV, RJTV, TVTV, RJRJ) are around 0.1 and that for the HSV is around 0.25. The large jump in the figure represents a state change from a TV or RJTV or HSV to an FC. The air flow rate coefficient C_q is just sufficient to make a TV or RJTV or HSV for low $Fr = 3.6$–7.3, but is not sufficient to make an RJRJ or a TVTV supercavity for high $Fr = 9.2$–12.9. Instead, an FC is formed, which results in a high σ_c around 0.9. Figure 29(*a*,*b*) shows the relationship between C_q and σ_c for various Fr, for all states and the supercavity states of the HSV, TV, RJTV, TVTV and RJRJ, respectively. For a given Fr, it is seen that a minimum cavitation number ($\sigma_{c,min}$) exists, regardless of an increase in C_q (figure 29*b*). The values are $\sigma_{c,min} = 0.14$, 0.13, 0.123, 0.12 for $Fr = 3.6$, 5.5, 7.3, 9.2, respectively. In addition, with a variation of C_q, there exists a minimum Froude number ($Fr = 7.3$) for supercavity states to be maintained without jumping to non-supercavitating states. In figure 30, the dimensionless length (l/d_c), height (h/d_c) and width (w/d_c) of the RJRJ supercavity (inner-layer ellipsoid) with a reentrant jet are plotted according to σ_c. To understand why the double-layer supercavities occur in case 4, let us consider figures 15(*b*) (case 2) and 29(*b*) (case 4), which are C_q versus σ_c diagrams for several Fr values. In figure 31, data from figures 15(*b*) and 29(*b*) are drawn altogether. It appears that case 4 data fill the C_q versus σ_c diagram of case 2 in a complementary way. If there were no operational restrictions on V, Q or mechanical restrictions (e.g. the control of the submergence depth) such that the ranges of the relevant dimensionless numbers were comparable to each other, they would collapse onto the

https://doi.org/10.1017/jfm.2018.638 Published online by Cambridge University Press

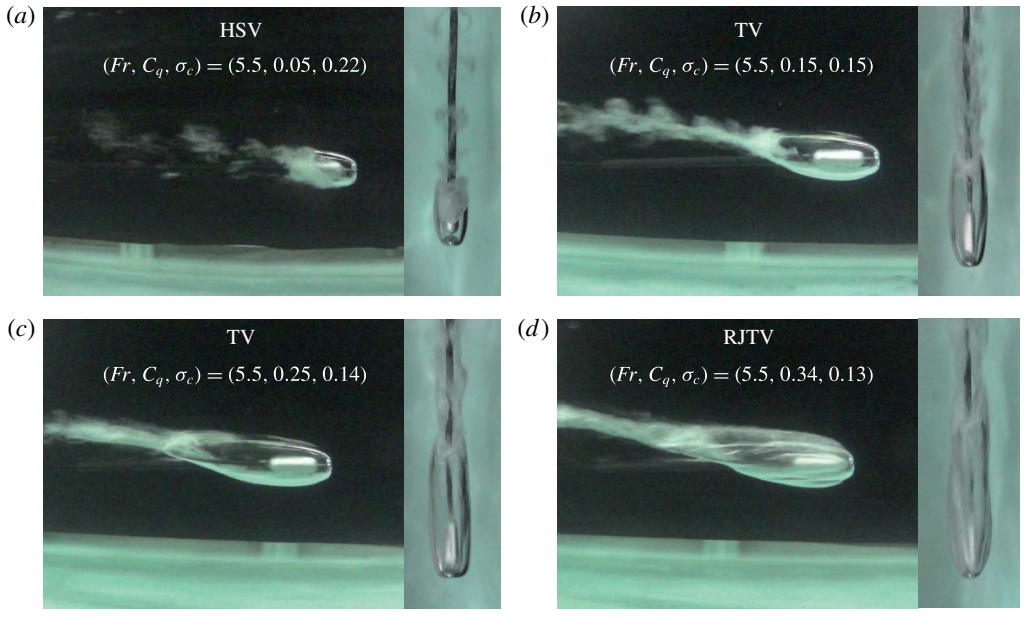

FIGURE 25. (Colour online) Side view and top view observations of steady-state phenomena around a fully submerged moving body with a large blockage ratio at various C_q ($C_q = 0.05$, 0.15, 0.25, 0.34) for a constant Froude number ($Fr = 5.5$); case 4 ($B = 3\,\%$, $h^* = 0.5$) in table 1.

same curve although each point on the diagram may represent a different supercavity state. In other words, for the same Fr and C_q, the resultant supercavities in cases 2 and 4 will have the same value of σ_c. The resultant supercavity shapes, however, could be different. The difference comes from the different blockage ratios B; $B = 3\,\%$ of case 4 is twice that $B = 1.5\,\%$ of case 2. Further, figure 32 shows both data from figures 16 (case 2) and 30 (case 4) together, which are the dimensionless cavity length, height and width data according to σ_c for the resultant RJ- and RJRJ-type supercavities, respectively; for the RJRJ-type supercavity, the inner-layer ellipsoid is considered. Again, data for cases 2 and 4 appear complementary to each other, and would collapse onto the same curve if the ranges of the relevant dimensionless numbers were comparable to each other. In other words, for the same σ_c, the larger blockage case 4 will admit a double-layer RJRJ supercavity instead of a single-layer RJ supercavity which may occur if there were no constraint on σ_c. In this particular case (a closed-shaped RJ supercavity), the resultant supercavities in cases 2 and 4 will have the same dimensionless ellipsoidal shapes. This reasoning can be checked from figure 44 in the Appendix, where the different supercavity shapes are shown for the similar values of (Fr, C_q, σ_c) for cases 2 and 4.

4. Drag measurement

In the experiment, the drag force (F_D) for a moving body with a speed V is obtained indirectly from the power consumption P for the RC-car run; $F_D = P/V$. The power consumption (P = voltage × current) is measured using a voltage sensor (Quanum TC9400, Operation range: 0–45 V, error $< \pm 1\,\%$) and a current sensor (Quanum ACS755 LCB-100, operation range: 0–100 A, error $< \pm 1\,\%$) which are schematically

https://doi.org/10.1017/jfm.2018.638 Published online by Cambridge University Press

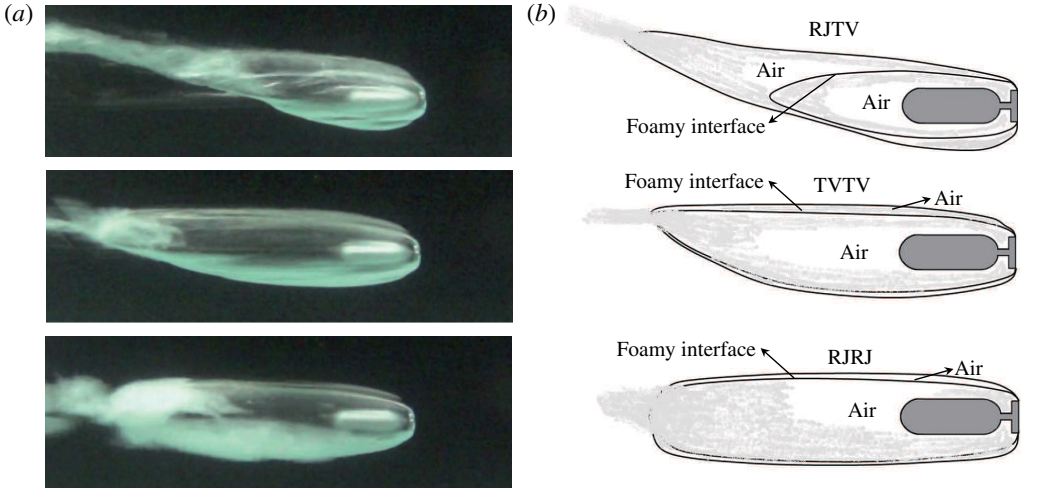

FIGURE 26. (Colour online) RJTV, TVTV and RJRJ supercavities (from top to bottom). (*a*) Photo shots, (*b*) illustrations based on photo shots.

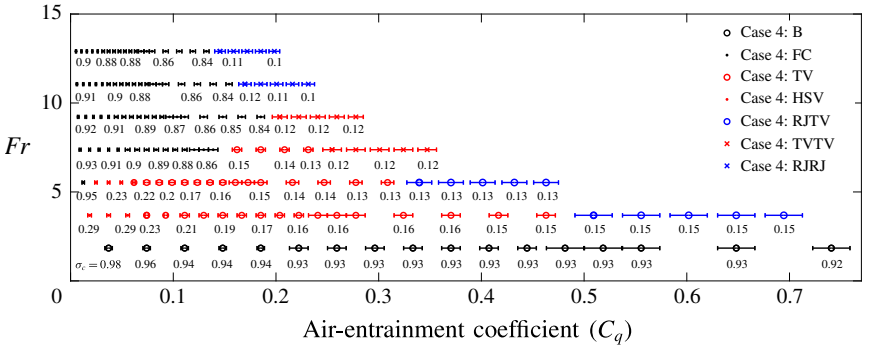

FIGURE 27. (Colour online) Air-entrainment coefficient (C_q) versus Froude number (Fr) for various steady states for case 4 ($B = 3\,\%$, $h^* = 0.5$) in table 1.

shown in figure 33. In the figure, the RC car is represented by the driving motor (M). Before the measurement of drag forces of the moving body in cases 1–4, we performed a preliminary test for the drag coefficients of moving spheres in water or air. In figure 34, as a first step, we measure the power consumption (P_1) required to move the sphere-attached carriage system with a speed V in water or air. Next, we measure the power consumption (P_2) required to move the sphere-removed carriage system with the same speed V in water or air. As already stated in § 2 (describing the experimental set-up), the support structure (cylindrical rod with a diameter of 10 mm) is C-shaped or positioned downstream so that there will be little influence on the flow upstream where a body exists. However, there will be a contribution to the drag force due to the vortex shedding. All the frictional and pressure drags, including this vortex-induced drag force during the translational motion with a speed V, are collectively and completely considered in the power consumption. Then, the

https://doi.org/10.1017/jfm.2018.638 Published online by Cambridge University Press

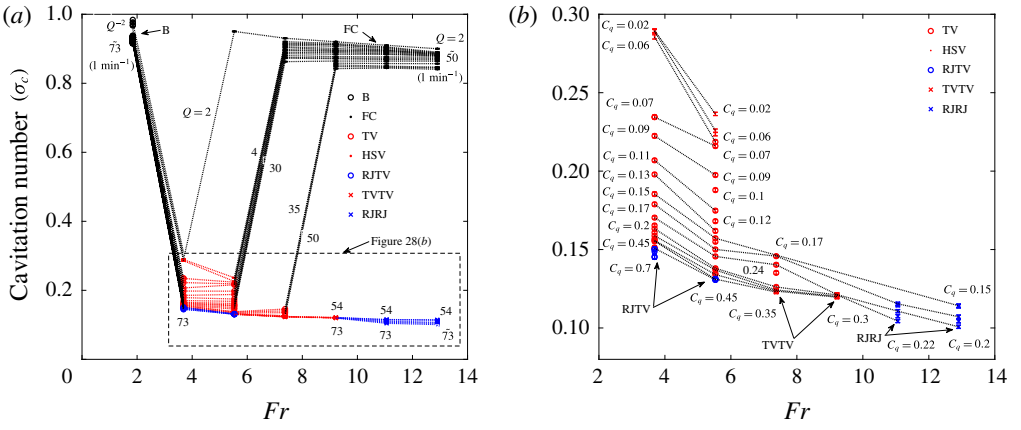

FIGURE 28. (Colour online) Froude number (Fr) versus cavitation number (σ_c) for case 4 ($B = 3\,\%$, $h^* = 0.5$) in table 1. (a) All states, (b) TV, HSV, RJTV, TVTV, RJRJ.

drag force F_D of the sphere only can be obtained as follows;

$$F_D = \frac{P_1 - P_2}{V}. \tag{4.1}$$

Then, if the diameter of the moving sphere is d_s in the fluid (density: ρ), the frontal-area-based drag coefficient C_d can be obtained as follows;

$$C_d = \frac{F_D}{\frac{1}{2}\rho V^2 \left(\frac{\pi}{4} d_s^2\right)}. \tag{4.2}$$

The resultant C_d obtained using (4.1) and (4.2) is shown in figure 35, according to the diameter-based Reynolds number $Re_{d_s} = Vd_s/\nu$ (ν: kinematic viscosity of the fluid). For comparison, figure 35 (solid curve) shows the well-known experimental results for the identically defined C_d (Goldstein 1938). As shown, for the Re_{d_s} range in the present experimental setting ($70\,000 < Re_{d_s} < 210\,000$), they agree with each other very well. In a similar way to the preliminary sphere test, we measured the drag coefficient C_d for cases 1–4. For example, for a moving body with a reentrant-jet supercavity, we performed four separate tests to obtain the drag coefficients (figure 36*a–c*). First, we measured the power consumption P_1 for moving the whole carriage system with a body attached, around which a reentrant-jet supercavity is formed (figure 36*b*) in water:

$$P_1 = P_{RC\,car} + P_{c\text{-}shaped\,rod} + P_{body\,with\,a\,supercavity}. \tag{4.3}$$

Next, after removing the supercavitating part (body plus rod), we performed the running test in water and measured the power consumption P_2 (figure 36*b*):

$$P_2 = P_{RC\,car} + P_{cut\,c\text{-}shaped\,rod,\,water}. \tag{4.4}$$

By subtracting (4.4) from (4.3), $P_1 - P_2$, we can calculate the power consumption for the body plus the supercavity plus the rod inside the supercavity (figure 36*b*).

https://doi.org/10.1017/jfm.2018.638 Published online by Cambridge University Press

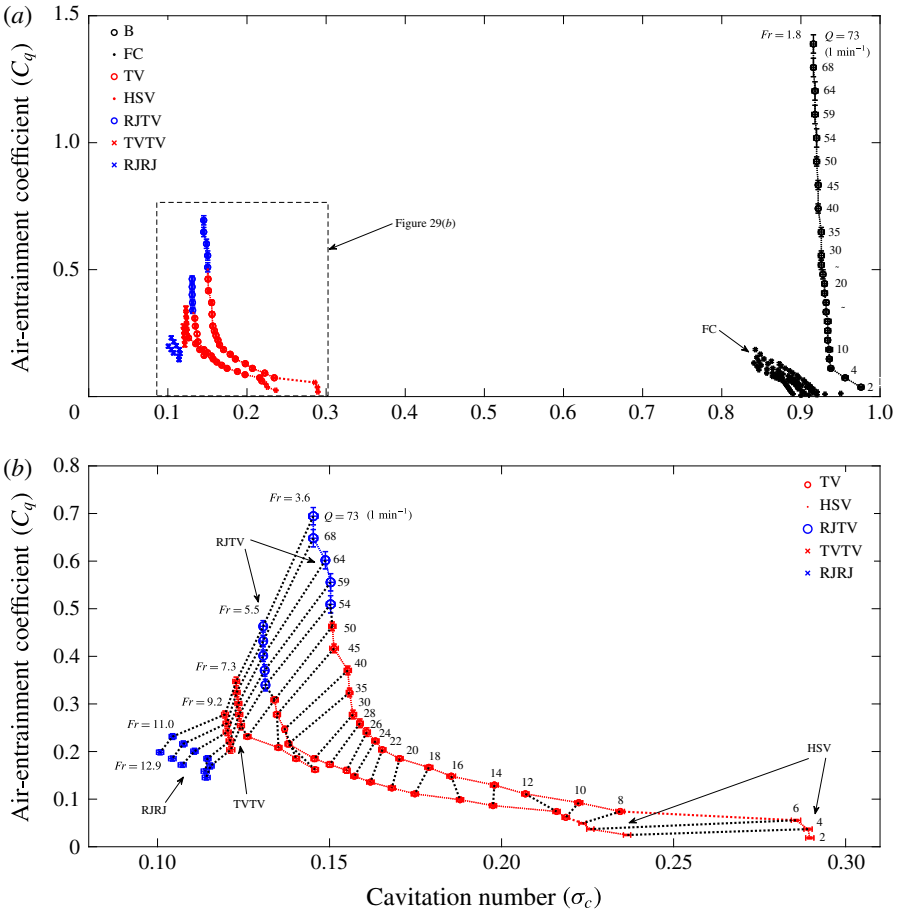

FIGURE 29. (Colour online) Cavitation number (σ_c) versus air-entrainment coefficient (C_q) for case 4 ($B = 3\,\%$, $h^* = 0.5$) in table 1. (*a*) All states, (*b*) TV, HSV, RJTV, TVTV, RJRJ.

To remove the effect of the rod inside the air-filled supercavity, we performed the running test without a body in the air as shown in figure 36(*c*) and measured the power consumption P_3 (figure 36*c*)

$$P_3 = P_{RC\,car} + P_{c\text{-}shaped\,rod,\,air}. \tag{4.5}$$

Then, similar to (4.4), but in the air, we performed the running test and measured the power consumption P_4 (figure 36*c*)

$$P_4 = P_{RC\,car} + P_{cut\,c\text{-}shaped\,rod,\,air}. \tag{4.6}$$

By subtracting (4.6) from (4.5), $P_3 - P_4$, we can calculate the power consumption for the rod inside the supercavity (figure 36*c*). From (4.3)–(4.6), for the moving body (speed: V) with a supercavity (figure 36*a*), the required power consumption (P) will be

$$P = P_1 - P_2 - (P_3 - P_4). \tag{4.7}$$

https://doi.org/10.1017/jfm.2018.638 Published online by Cambridge University Press

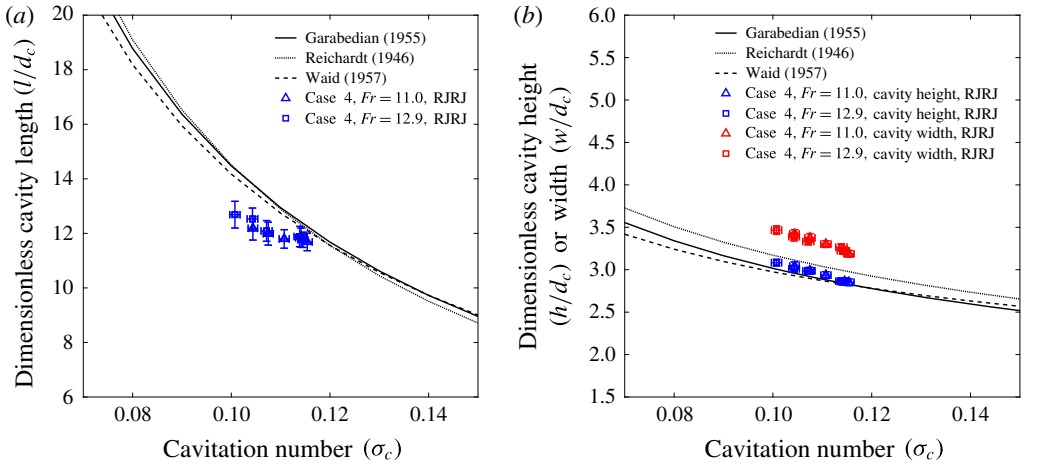

FIGURE 30. (Colour online) Normalized length (l/d_c), height (h/d_c) and width (w/d_c) of the supercavity according to σ_c, where d_c is the diameter of the cavitator. (*a*) Normalized length, (*b*) normalized height and width; case 4 ($B = 3\,\%$, $h^* = 0.5$) in table 1.

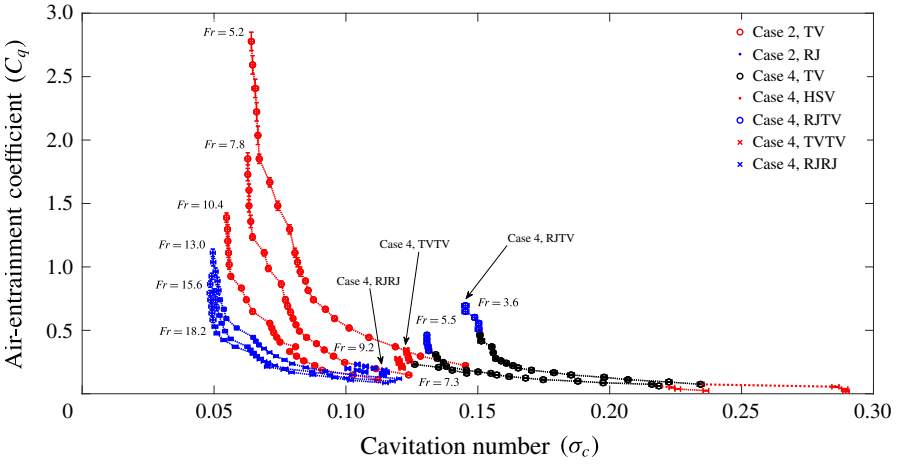

FIGURE 31. (Colour online) Cavitation number (σ_c) versus air-entrainment coefficient (C_q) for case 2 ($B = 1.5\,\%$, $h^* = 0.5$) and case 4 ($B = 3\,\%$, $h^* = 0.5$) in table 1.

Then, the drag force F_D can be obtained as follows:

$$F_D = \frac{P}{V}. \tag{4.8}$$

Finally, the body-frontal-area-based drag coefficient is calculated:

$$C_d = \frac{F_D}{\frac{1}{2}\rho V^2 \left(\frac{\pi}{4}d^2\right)}. \tag{4.9}$$

In this way, all the drag coefficients C_d for cases 1–4 are obtained, and the results are summarized in figures 37 and 38. In figure 37(*a–d*), the cavitation number σ_c versus

https://doi.org/10.1017/jfm.2018.638 Published online by Cambridge University Press

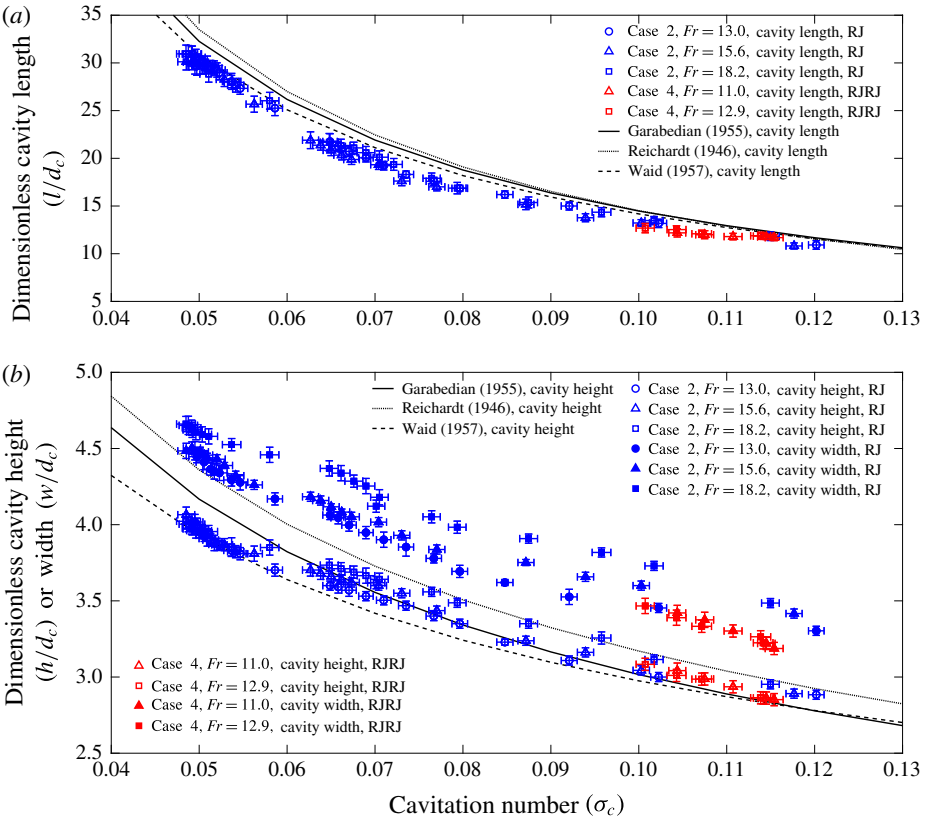

FIGURE 32. (Colour online) Normalized length (l/d_c), height (h/d_c) and width (w/d_c) of the reentrant-jet supercavity according to σ_c for case 2 ($B = 1.5\,\%$, $h^* = 0.5$) and case 4 ($B = 3\,\%$, $h^* = 0.5$) in table 1. (*a*) Normalized length, (*b*) normalized height and width.

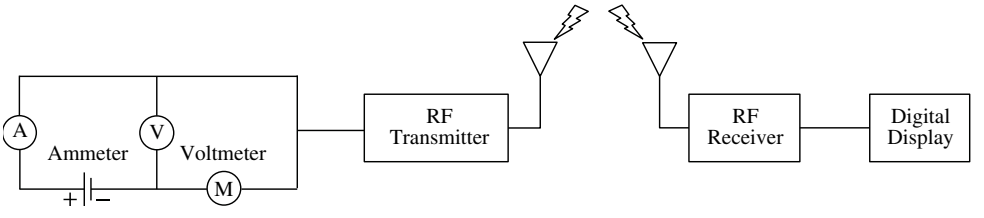

FIGURE 33. Measurement of power consumption ($P =$ voltage $\times$ current).

drag coefficient C_d is shown depending on the Froude number Fr_d (case 1) or Fr (cases 2–4), respectively. The vertical axes have been rescaled to accentuate the minute variation in C_d, all of which lie within about 4 % of the mean value for each case. In figure 38, the drag coefficient C_d in figure 37(*a–d*) is replotted according to the body-diameter-based Reynolds number Re_d for all cases 1–4. For a non-supercavitating body with a cavitator (cases 2–4), the drag coefficient C_d is approximately 1.15. Note that this number is very close to the well-known $C_d = 1.17$ of the disk (White 1999). For a non-supercavitating body without a cavitator (case 1), the drag coefficient C_d is approximately 0.4. For a supercavitating body (TV, RJ, RJTV, TVTV, RJRJ) in

https://doi.org/10.1017/jfm.2018.638 Published online by Cambridge University Press

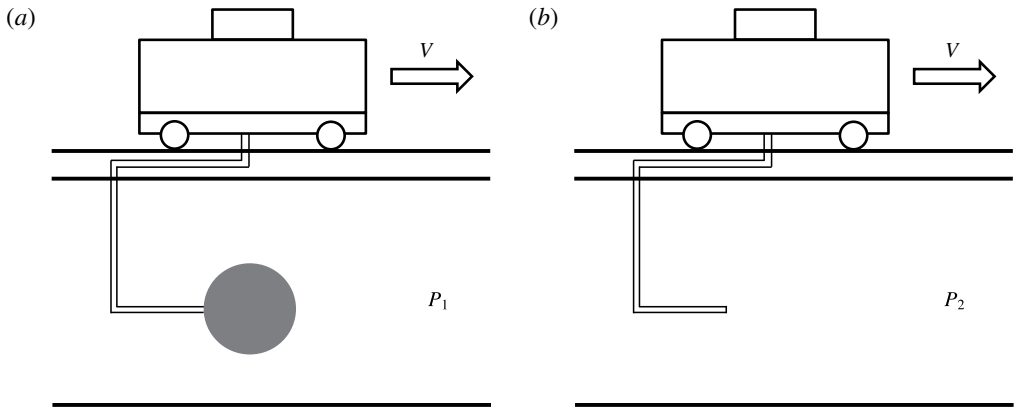

FIGURE 34. Measurement of power consumption required to move the carriage system with a speed V. (a) With a sphere, (b) without a sphere.

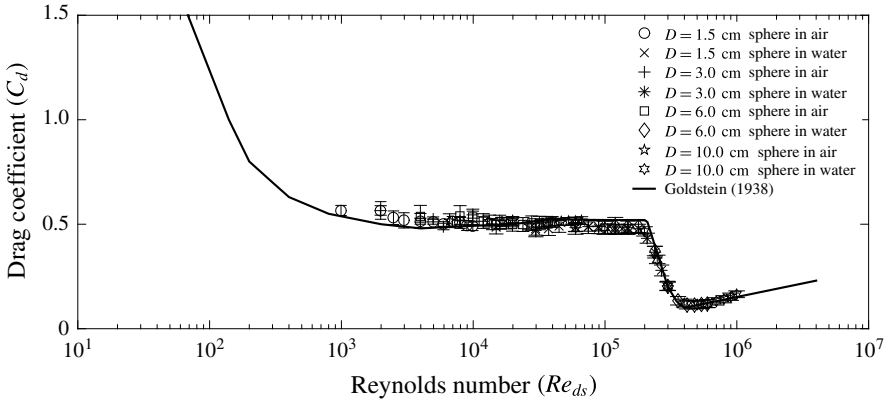

FIGURE 35. Frontal-area-based drag coefficient $C_d = F_D/[(1/2)\rho V^2(\pi/4d_s^2)]$ according to the diameter-based Reynolds number $Re_{d_s} = Vd_s/\nu$ (ν: kinematic viscosity of the fluid). The solid curve comes from Goldstein (1938).

cases 2–4, the drag coefficient C_d is approximately 0.11. By comparing the case where C_d is approximately 0.4 (a non-supercavitating body without a cavitator) and the case where C_d is approximately 1.15 (a non-supercavitating body with a cavitator), in the case of no supercavity, we see that the existence of the cavitator has a negative effect on the drag reduction. However, as seen from the case where C_d is approximately 0.11 (a supercavitating body with TV, RJ, RJTV, TVTV, RJRJ supercavities), the just-mentioned negative effect of a cavitator is noticeably compensated by the generation of a supercavity, which plays a significant role by reducing C_d by approximately 73 % (=(0.4 − 0.11)/0.4) compared to the case where C_d is approximately 0.4, and approximately 90 % (= (1.15 − 0.11)/1.15) compared to the case where C_d is approximately 1.15.

To analyse the experimental results of the drag measurement, let us consider the control volume in figure 39, where the reference frame is attached to the moving body. The control volume is composed of a surface at upstream infinity (S_u), a stream tube at infinity, the annular surface (S) at the location of the maximum cavity height

https://doi.org/10.1017/jfm.2018.638 Published online by Cambridge University Press

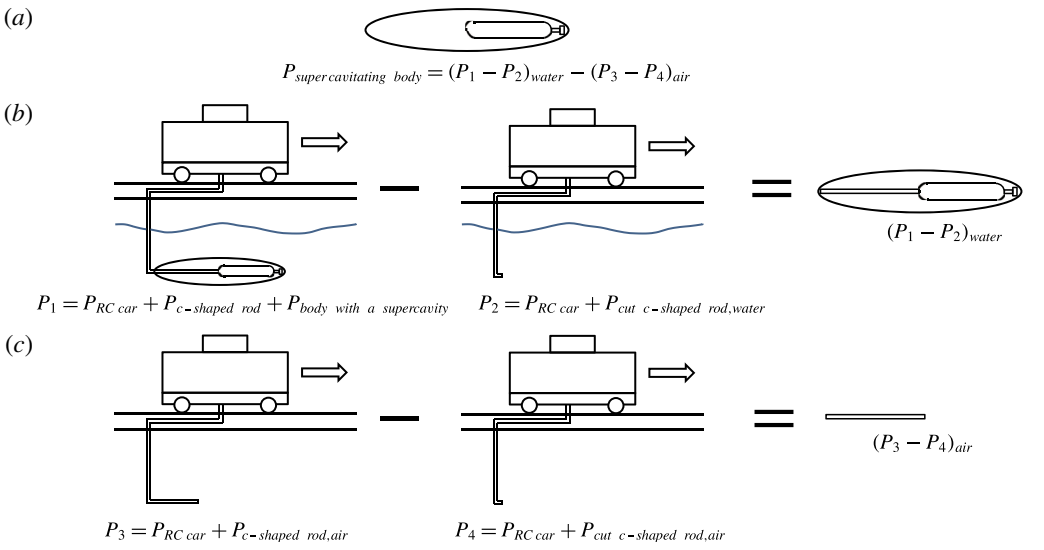

FIGURE 36. Schematics for the calculation of power consumption of a supercavitating moving body with speed V. (*a*) A supercavitating moving body, (*b*) a supercavitating moving body plus a cut rod inside the supercavity, (*c*) cut rod inside the supercavity.

and the cross-sectional surface (S_c) at the location of the maximum cavity height. The following analysis is based on the work of Franc & Michel (2004). From the mass conservation,

$$\rho V S_u = \int_s \rho U_a \, \mathrm{d}A. \tag{4.10}$$

From the linear momentum theorem,

$$F_D - p_\infty (S + S_c) + p_c S_c + \int_s p \, \mathrm{d}A = \rho V^2 S_u - \int_s \rho U_a^2 \, \mathrm{d}A, \tag{4.11}$$

where F_D is the drag force to the cavitating body. By combining (4.10) and (4.11),

$$F_D = (p_\infty - p_c) S_c - \int_s (p - p_\infty) \, \mathrm{d}A + \int_s \rho U_a (V - U_a) \, \mathrm{d}A. \tag{4.12}$$

Now, from the Bernoulli equation,

$$p + \tfrac{1}{2}\rho (U_a^2 + U_r^2) = p_\infty + \tfrac{1}{2}\rho V^2, \tag{4.13}$$

where U_r is the radial velocity. Then, from (4.12) and (4.13),

$$F_D = (p_\infty - p_c) S_c - \frac{\rho}{2} \int_s (V - U_a)^2 \, \mathrm{d}A + \frac{\rho}{2} \int_s \rho U_r^2 \, \mathrm{d}A. \tag{4.14}$$

Since $V \approx U_a$ and U_r is zero on the cavity and also zero on S from the differential analysis (Franc & Michel 2004), the second and third terms disappear. Then, equation (4.14) is reduced to

$$F_D \approx (p_\infty - p_c) S_c. \tag{4.15}$$

https://doi.org/10.1017/jfm.2018.638 Published online by Cambridge University Press

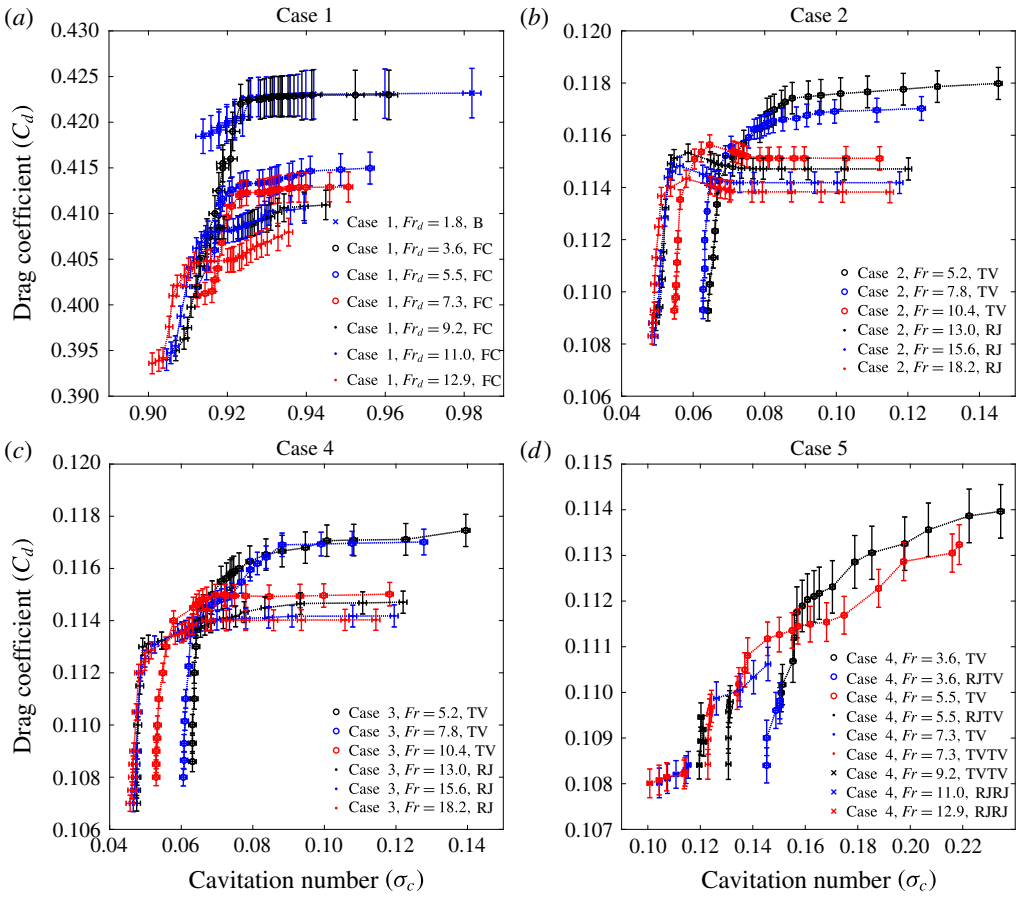

FIGURE 37. (Colour online) Drag coefficient C_d of moving bodies (cases 1–4) according to the cavitation number σ_c and the Froude number Fr_d (case 1) or Fr (cases 2–4).

By applying (4.15) to our non-circular cavity,

$$F_D = \frac{\rho V^2}{2}\sigma_c \frac{\pi}{4} wh. \tag{4.16}$$

Then, the drag coefficient based on the body frontal area is

$$C_d = \frac{F_D}{\dfrac{\rho V^2}{2}\dfrac{\pi}{4}d^2} = \frac{\sigma_c}{d^2} wh. \tag{4.17}$$

By using (3.6) and (3.7) for h and w in case 2 and (3.19) and (3.20) for h and w in case 3, we calculated C_d according to σ_c and the results are plotted in figure 40. The range of C_d is between 0.11 and 0.21 or, on average, 0.16 ± 0.05, which is larger than the measured $C_d = 0.1$.

As a final remark in this section, we do not include the power required to deliver the air flow to the cavity in the calculation of C_d. The reason is twofold. First, the measured power (P) is for the drag force $F_D = P/V$ for a 'moving' body with a

https://doi.org/10.1017/jfm.2018.638 Published online by Cambridge University Press

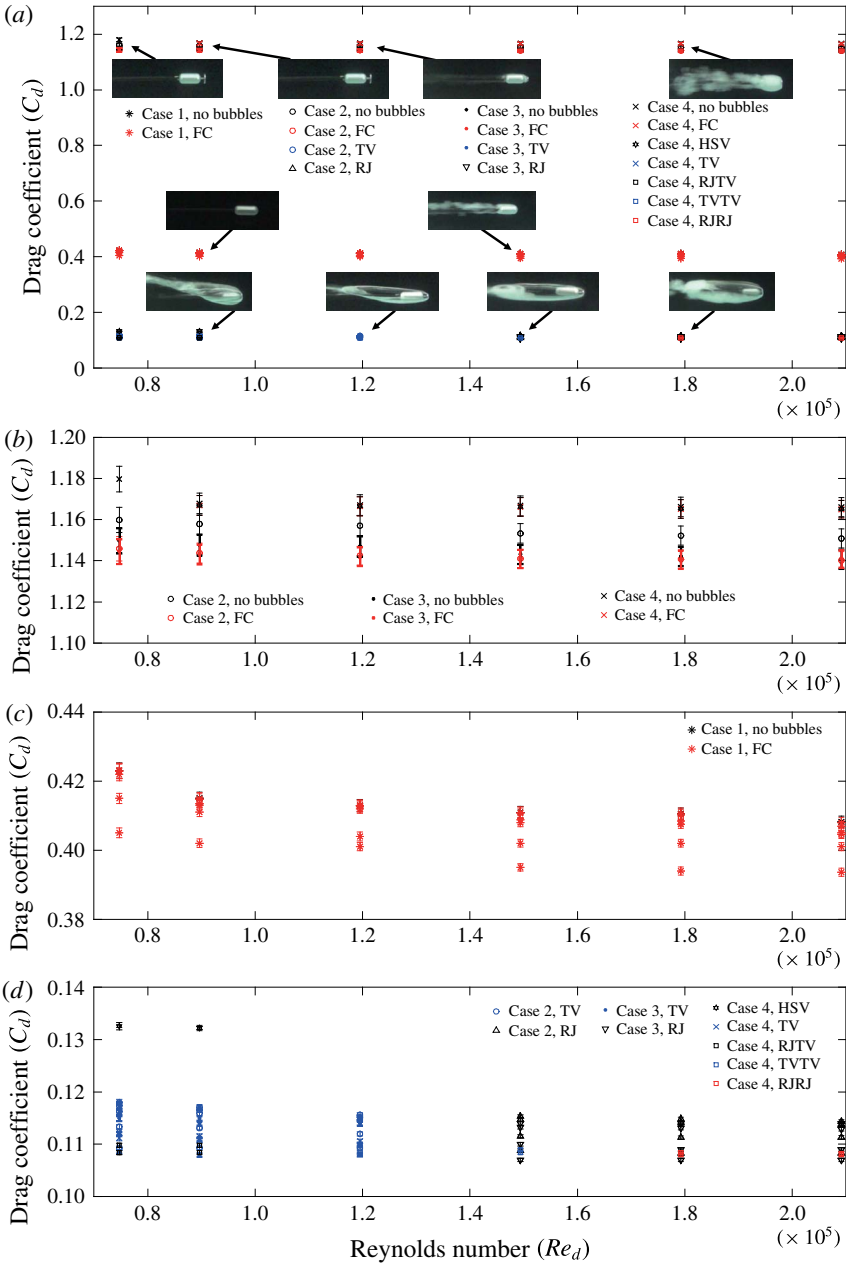

FIGURE 38. (Colour online) Drag coefficient C_d of moving bodies (cases 1–4) according to the body-diameter-based Reynolds number Re_d. (*a*) Overall Re_d versus C_d diagram, (*b*) Re_d versus C_d diagram near $C_d = 1.15$, (*c*) Re_d versus C_d diagram near $C_d = 0.4$, (*d*) Re_d versus C_d diagram near $C_d = 0.11$.

speed V, whether the case is supercavitating or non-supercavitating. In other words, for a moving supercavitating body, we assume that the supercavity is already there. Second, the power to deliver the air flow through a channel (in our case, smooth

https://doi.org/10.1017/jfm.2018.638 Published online by Cambridge University Press

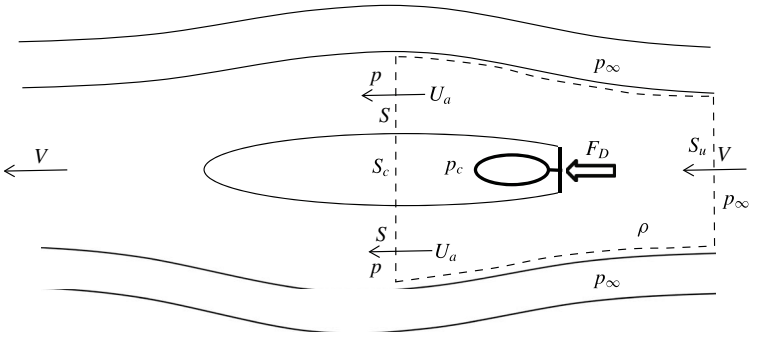

FIGURE 39. A control volume for the analysis of the drag. The control volume is composed of a surface at upstream infinity (S_u), a stream tube at infinity, the annular surface (S) at the location of the maximum cavity height and the cross-sectional surface (S_c) at the location of the maximum cavity height.

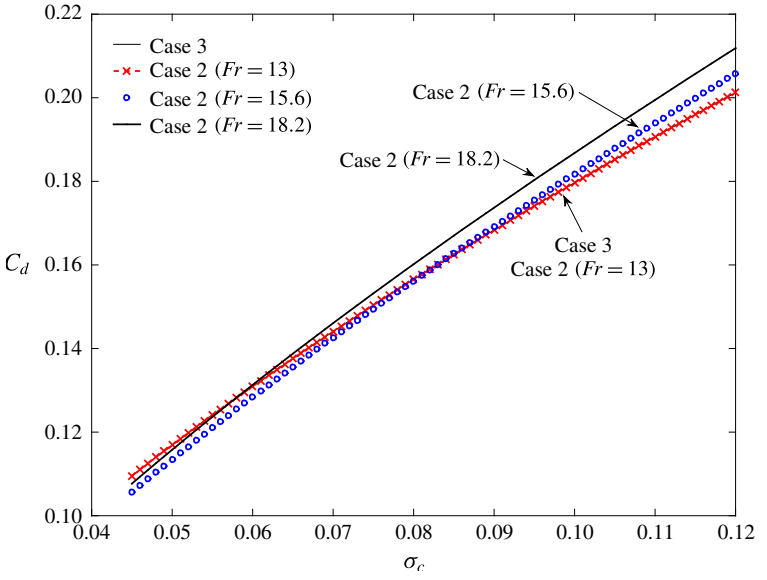

FIGURE 40. (Colour online) Theoretical drag coefficients C_d for the RJ supercavities in cases 2 and 3, using (4.17).

tube) is proportional to the length of the channel whether the flow inside the channel is laminar or turbulent. This means that, depending on the position of the source of the compressed air, the power will be different. For our case (circular tube), if the volume flow rate of the air is Q, then the relevant Reynolds number (based on the tube diameter D, and the average air speed $\overline{V}$ inside the tube) will be

$$Re_D = \frac{\rho_a \overline{V} D}{\mu_a} = \frac{\rho_a D}{\mu_a} \frac{Q}{\pi D^2/4} = \frac{4\rho_a Q}{\pi D \mu_a}, \tag{4.18}$$

where ρ_a is the density of air and μ_a is the dynamic viscosity of air. Depending on the value of Re_D, one can calculate the required power ($P_{air\ delivery}$) to deliver the air

https://doi.org/10.1017/jfm.2018.638 Published online by Cambridge University Press

through the tube (length: L) as follows (White 1999):

$$P_{air\ delivery} = \frac{8\rho_a f L Q^3}{\pi D^4}, \tag{4.19}$$

where f is the Darcy friction factor which is calculated as follows

$$f = \begin{cases} \dfrac{64}{Re_D} & \text{Laminar } (Re_D < 2300) \\ \dfrac{1}{\left[-1.8\log_{10}\left(\dfrac{6.9}{Re_D} + \left(\dfrac{\epsilon/D}{3.7}\right)^{1.11}\right)\right]^2} & \text{Turbulent } (Re_D > 2300) \text{ (Haaland 1983),} \end{cases} \tag{4.20}$$

where ϵ is the roughness of the tube. Equations (4.19) and (4.20) are applied to the smooth-wall ($\epsilon = 0$) tubes with length $L = 75$ mm (body length). For example, figure 41 shows the powers for the motions (4.7) in case 2, the power for the motion of the body without a cavitator and the power for the air delivery for $L = 75$ mm. As an example, for $Q = 75$ l min^{-1} and $Re_d = 20\,9200$, the power reduction is 34.5 W (47.6 W − 13.1 W = 34.5 W) and the power for the air delivery for $L = 75$ mm is 3.3 W so that 9.5 % (= 3.3/34.5) of the power reduction is expended in the delivery of air to the cavity. For $L = 20$ m (our real experimental setting), the power for the air delivery is 883 W, and we do not think that the comparison is fair. In the application of a real supercavitating torpedo, some of the exhausted gas can be used as the source for the formation of supercavity, thus requiring a very short passage for the gas or little power for the delivery of air to the cavity like the just-mentioned example for $L = 75$ mm.

5. Summary and discussion

5.1. *Summary*

Present experimental study examines ventilated supercavity formation in a free-surface bounded environment where the body is in motion and the fluid is at rest. For a given torpedo-shaped (a cylinder capped with hemispherical ends) body (diameter: d) and water depth (H), depending on the existence of a cavitator, the cavitator diameter (d_c) and the submergence depth (h_s), seven different cases are investigated according to the dimensionless cavitator size ($d^* = d_c/d$), the blockage ratio ($B = d_c/d_h$; d_h is the hydraulic diameter) and the dimensionless submergence depth ($h^* = h_s/H$). When a body exists ($d \neq 0$), cases 1–4 are, respectively, (d^*, B, h^*) = (0, 0, 0.5), (0.5, 1.5 %, 0.5), (0.5, 1.5 %, 0.17), (1, 3 %, 0.5). When no body exists ($d = 0$), case 5–7 are, respectively, (d^*, B, h^*) = (∞, 1.5 %, 0.5), (∞, 1.5 %, 0.17), (∞, 3 %, 0.5). We found that the overall phenomena in cases 2–4 are almost the same as those in cases 5–7. In other words, the existence of a body affects only little the flow phenomena. Therefore, only cases 1–4 are considered, since we are also interested in the drag reduction by comparing a supercavitating moving body with a non-supercavitating moving body. Overall, nine steady states are observed according to the relevant Froude numbers (Fr), the air-entrainment coefficients (C_q) and the cavitation number (σ_c); bubbly flow (B), a foamy cavity (FC), a half-supercavity with foamy cavity downstream (HSF), a twin-vortex supercavity (TV), a reentrant-jet supercavity (RJ), a half-supercavity with a ring-type vortex shedding downstream (HSV), a double-layer supercavity with a

https://doi.org/10.1017/jfm.2018.638 Published online by Cambridge University Press

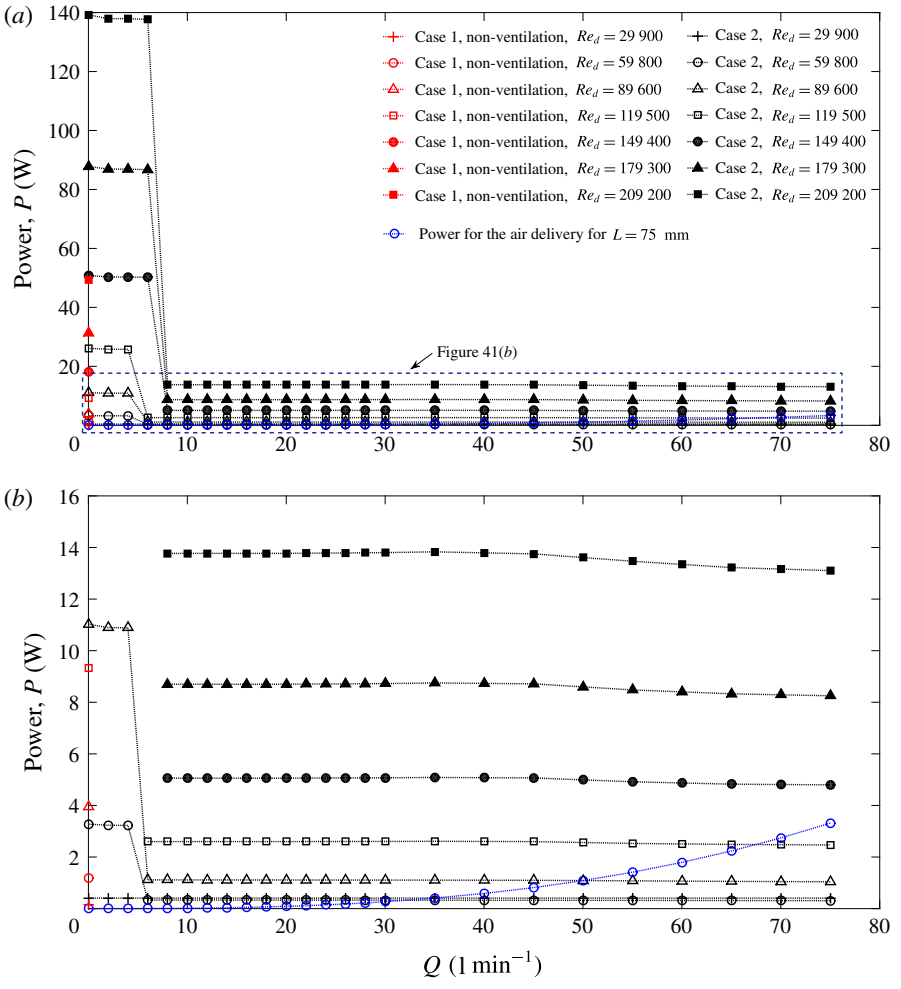

FIGURE 41. (Colour online) Powers for the motions (P in (4.7)) for ventilated case 2, non-ventilated case 1 and the powers for the air delivery for $L = 75$ mm.

reentrant jet inside and twin vortices outside (RJTV), a double-layer supercavity with twin vortices inside and twin vortices outside (TVTV), a double-layer supercavity with a reentrant jet inside and a reentrant jet outside (RJRJ).

(i) Case 1 ($B = 0$, $h^* = 0.5$): B, FC.
(ii) Case 2 ($B = 1.5\,\%$, $h^* = 0.5$): B, FC, HSF, TV, RJ.
(iii) Case 3 ($B = 1.5\,\%$, $h^* = 0.17$): B, FC, HSF, TV, RJ.
(iv) Case 4 ($B = 3\,\%$, $h^* = 0.5$): B, FC, HSV, TV, RJTV, TVTV, RJRJ.

The cavitation numbers (σ_c) are approximately 0.9 for the B, FC, HSF, 0.25 for the HSV, and 0.1 for the TV, RJ, RJTV, TVTV, RJRJ. For cases 2–4, the ranges of (Fr, C_q, σ_c) are as follows; $Fr = 2.6$–18.2, $C_q = 0$–6, $\sigma_c = 0$–1 for cases 2 and 3, $Fr = 1.8$–12.9, $C_q = 0$–1.5, $\sigma_c = 0$–1 for case 4. In all cases 2, 3 and 4, for a given Fr, there exists a minimum cavitation number $\sigma_{c,min}$ in the formation of a supercavity. Also, $\sigma_{c,min}$ decreases as the Fr increases. Case 2 ($B = 1.5\,\%$, $h^* = 0.5$) and case 3

https://doi.org/10.1017/jfm.2018.638 Published online by Cambridge University Press

($B = 1.5\,\%$, $h^* = 0.17$) are different in terms of the closeness to the free surface. In cases 2 and 3, both TV and RJ supercavities are observed. A high Fr favours an RJ and a low Fr favours a TV. This is different from the case of a closed environment (Karn *et al.* 2016) where high C_q and Fr favours a TV and low C_q and Fr favours an RJ. Also, supercavities in case 3 are not top–bottom symmetric. For ellipsoidal RJ supercavities in cases 2 and 3, the cavity cross-section is a fat ellipse, i.e. the cavity width is always larger than the cavity height. In addition, the cavity length, height and width all increase (decrease) as σ_c decreases (increases). The cavity length in case 3 is smaller than that in case 2. In both cases 2 and 3, the cavity length does not depend on the Fr. In case 2, the cavity height and width increase as the Fr increases. In case 3, the cavity height and width show a weak dependence on the Fr or show a good collapse onto each other. In both cases 2 and 3, the cavity length, height and width data are compared with existing studies and are shown to, for the most part, agree with each other. Like existing studies, we also suggest the empirical formulas for the length, height and width data for cases 2 and 3. Case 2 ($B = 1.5\,\%$, $h^* = 0.5$) and case 4 ($B = 3\,\%$, $h^* = 0.5$) are different in terms of the blockage ratio. In case 4, we found diverse supercavities (RJTV, TVTV, RJRJ) which are not observed in case 2. For RJ (case 2) and RJRJ (case 4) supercavities, the cavity length, height and width data according to σ_c collapse onto the same curve. In other words, for the same σ_c, case 4 admits a double-layer RJRJ supercavity instead of a single-layer RJ supercavity which may occur if there is no constraint on σ_c. As stated in the introduction, Campbell & Hilborne's (1958) work is very close to the present experimental study. Their work was carried out in a circular free-surface water channel (water depth: 0.46 m, channel width: 0.91 m, submergence depth: 0.22 m) with disk-type cavitators (diameter: 0.013 m, 0.019 m, 0.025 m, blockage ratio $B = 1.4\,\%$, $2.1\,\%$, $2.8\,\%$, $h^* = 0.47$) although they did not consider the effect of the closeness to the free surface on the formation of a supercavity. Our case 2 ($B = 1.5\,\%$, $h^* = 0.5$) and case 4 ($B = 3\,\%$, $h^* = 0.5$) are similar to some of their cases ($B = 1.4\,\%$, $h^* = 0.47$ and $B = 2.8\,\%$, $h^* = 0.47$). They showed that an RJ supercavity occurs when $\sigma_c Fr > 1$ and TV supercavity occurs when $\sigma_c Fr < 1$. This does not agree with the present experimental study. In particular, for our cases 2 and 3, a high Fr favours an RJ and a low Fr favours a TV. For case 4 ($B = 3\,\%$, $h^* = 0.5$), we found diverse supercavities (RJTV, TVTV, RJRJ), which were not observed in their work for the similar conditions ($B = 2.8\,\%$, $h^* = 0.47$). Finally, the drag forces of various steady states found in cases 2–4 are measured and compared with each other according to the Reynolds numbers based on the body diameter, from which we found that the body-frontal-area-based drag coefficient for a moving body with a supercavity is approximately 0.11, while that for a cavitator-free moving body without a supercavity is approximately 0.4. Thus, the effect of supercavitation on the drag reduction (approximately $73\,\%$) can be clearly seen.

5.2. *Discussion*

Figure 42 shows the relationship between the minimum cavitation number ($\sigma_{c,min}$) and the Fr for various blockage ratios B for closed- and free-surface environments. The closed channel data are from Karn *et al.* (2016) and the free-surface channel data are from Campbell & Hilborne (1958), Kuklinski *et al.* (2001) and the present work. In the work of Karn *et al.* (2016), the channel is a closed square (0.19 m by 0.19 m) with disk-type cavitators at the centre of the channel ($B = 5\,\%$, $9\,\%$, $14\,\%$, $19\,\%$). In the work of Campbell & Hilborne (1958), the channel is a circular free-surface towing tank (water depth: 0.46 m, channel width: 0.91 m, submergence depth: 0.22 m) with

https://doi.org/10.1017/jfm.2018.638 Published online by Cambridge University Press

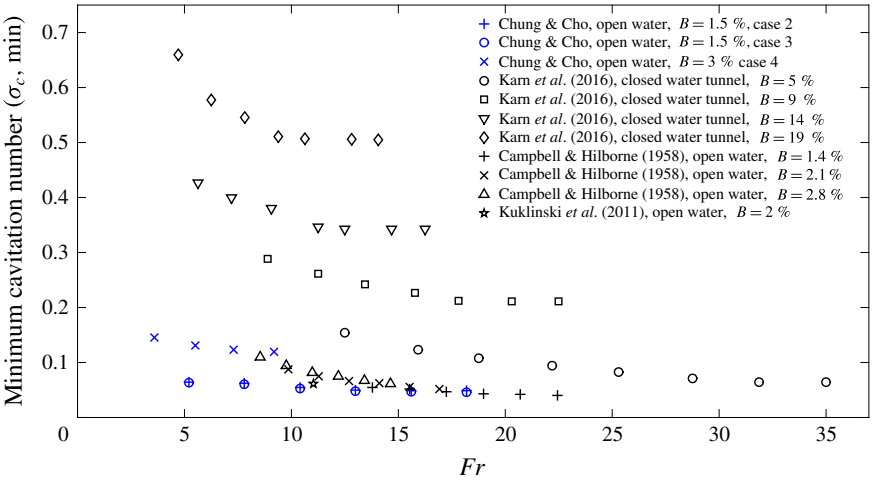

FIGURE 42. (Colour online) Relationship between $\sigma_{c,min}$ and Fr for various blockage ratios B for closed- and free-surface environments.

disk-type cavitators ($B = 1.4\,\%$, $2.1\,\%$, $2.8\,\%$ for $h^* = 0.47$). In the work of Kuklinski *et al.* (2001), the channel is a straight free-surface towing tank (water depth: 3.6 m, channel width: 7.3 m, no information about the submergence depth) with a disk-type cavitator ($B = 2\,\%$). In the present work, the channel is a straight free-surface towing tank (water depth: 0.5 m, channel width: 1 m) with case 2 ($B = 1.5\,\%$, submergence depth: 0.25 m or $h^* = 0.5$), case 3 ($B = 1.5\,\%$, submergence depth: 0.085 m or $h^* = 0.17$) and case 4 ($B = 3\,\%$, submergence depth: 0.25 m or $h^* = 0.5$). For the case of the closed water tunnel (Karn *et al.* 2016), for a given B, $\sigma_{c,min}$ decreases asymptotically to a certain non-zero value as the Fr increases (0.08, 0.21, 0.35, 0.51 at $Fr = 32$, 18, 14, 11 for $B = 5\,\%$, $9\,\%$, $14\,\%$, $19\,\%$). As B increases, the $\sigma_{c,min}$–Fr data curves are shifted upwards without crossing each other for different B cases. All $\sigma_{c,min}$–Fr data curves for the free-surface tunnel cases ($B = 1.4$–$3\,\%$) from Campbell & Hilborne (1958) are below the $\sigma_{c,min}$–Fr data for the $B = 5\,\%$ curve for the closed tunnel case. In free-surface tunnel cases, for a given B, $\sigma_{c,min}$ decreases as the Fr increases like the closed tunnel cases, asymptotically approaching a certain value close to zero. For our cases, based on the data in figure 42, the relationship between $\sigma_{c,min}$ and Fr is as follows;

$$\sigma_{c,min} = \begin{cases} \dfrac{0.12}{Fr^{0.32}} & (B = 1.5\,\%) \\ \dfrac{0.19}{Fr^{0.21}} & (B = 3\,\%). \end{cases} \tag{5.1}$$

Overall, the fact that $\sigma_{c,min}$ decreases as the Fr increases is common to both closed- and free-surface water tunnel cases. The difference is that, on the C_q–σ_c diagram, supercavities are possible all along the L-shaped curve in our case (figures 15*b*, 21*b* and 29*b*), but, are concentrated on the vertical branch in Karn *et al.*'s (2016) work.

Another difference between the closed- and free-surface water tunnel is the supercavity formation for similar blockage ratios ($B = 5\,\%$ case in Karn *et al.* (2016) and case 4 ($B = 3\,\%$, $h^* = 0.5$) in the present work). The closed water tunnel case

https://doi.org/10.1017/jfm.2018.638 Published online by Cambridge University Press

($B = 5\,\%$) in Karn *et al.* (2016) shows the FC, TVRJ, TVQV (twin-vortex quad-vortex closure), TV at relatively high *Fr* (20–40) and the RJ, QVRJ (quad-vortex reentrant-jet closure), QV (quad-vortex closure), PTV (pulsating twin-vortex closure) at relatively low *Fr* (0–40), according to increasing C_q (0.001–10). These several supercavity modes, the TVRJ, TVQV, QVRJ, PTV are unstable as observed at the transition of two stable closure modes. For a fair comparison with our case, if we confine the ranges to *Fr* (5–13) and C_q (0–0.7), then the FC, RJ, QVRJ, QV at high *Fr* (9–13) and the FC, QVRJ at low *Fr* (5–9) according to increasing C_q (0–0.7). Comparatively, case 4 ($B = 3\,\%$, $h^* = 0.5$) in the present work shows FC, RJRJ at high *Fr* (11–13), FC, TV, TVTV at intermediate *Fr* (7.3–9) and HSV, TV, RJTV at low *Fr* (3.6–5.5) according to increasing C_q (0–0.7). All these modes are stable steady states.

Although the supercavity formations for a similar B are quite different from each other between the closed- and free-surface water tunnel cases, the overall trend of favoured supercavity formation between the closed- and free-surface water tunnel cases may be similar. For the case of a closed water tunnel, Karn *et al.* (2016) posits that the closure mechanism is mainly determined by the pressure difference across the gas–water interface at the cavity closure. The relevant equation ((4.7) in Karn *et al.* (2016)) is as follows;

$$2\frac{p_{out} - p_{in}}{\rho V^2} = \Delta\widetilde{p} = \sigma_c(1 - 0.82B^2) - 0.82B^2, \tag{5.2}$$

where p_{in} and p_{out} are the pressures inside and outside the cavity at the closure. For the reentrant jet (RJ) supercavity, the $\Delta\widetilde{p}$ is dominated by the momentum of the reentrant water jet, while for a twin-vortex (TV) supercavity, the difference is much smaller, i.e. $\Delta\widetilde{p}_{RJ} \gg \Delta\widetilde{p}_{TV}$. Therefore, according to (5.2), a higher blockage (B) leads to a smaller $\Delta\widetilde{p}$, thus promoting the occurrence of a twin-vortex supercavity. This trend depending on B may be compared with our free-surface tunnel results considering case 2 ($B = 1.5\,\%$, $h^* = 0.5$) and case 4 ($B = 3\,\%$, $h^* = 0.5$). For a fair comparison, we confine the ranges of *Fr* (5–13) and C_q (0–0.5). Only RJ and TV supercavities are observed in case 2; an RJ at a high *Fr* (around 13) and a TV at a low *Fr* (5–10). On the other hand, an FC and TV, HSV, RJTV, TVTV, RJRJ supercavities are observed in case 4. At similar conditions to those making RJ supercavities in case 2, considerable FC and RJRJ are observed in case 4. At similar conditions to those making TV supercavities in case 2, TV variants (TVTV, RJTV) and HSV are observed in case 4. Overall, the survival rate of the TV family is higher than the RJ family when the blockage ratio becomes higher. In this regard, there may be a trend that a high blockage (B) leads to a TV supercavity in a free-surface environment.

As a final remark, many phenomena observed in the present experimental work are new, such as the *Fr* dependence of RJ supercavities in cases 2 and 3, and double-layer supercavities in case 4. Therefore, the physical explanation on these new phenomena requires some theoretical work which is left to future studies. We believe that our experimental study can provide both new and complimentary results which may have been overlooked in many existing experimental studies in cavitation tunnels where the body is at rest and the fluid is in motion in a bounded or closed environment.

Acknowledgement

This work was supported by the National Research Foundation of Korea (NRF) (NRF-2017R1D1A1B03028299).

https://doi.org/10.1017/jfm.2018.638 Published online by Cambridge University Press

Appendix. Overall comparison between cases 2 and 3 and between cases 2 and 4 for similar values of (Fr, C_q, σ_c)

These comparisons are shown in figures 43 and 44.

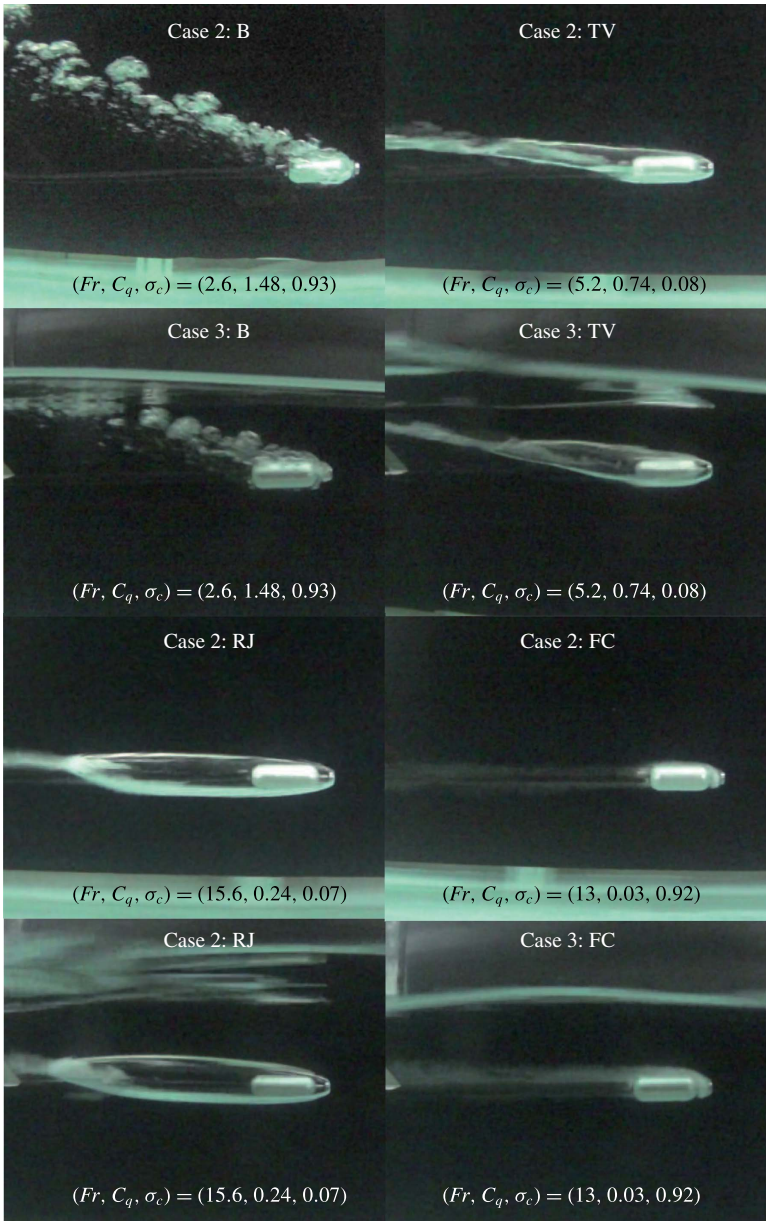

FIGURE 43. (Colour online) Side view observations of steady-state phenomena for similar values of $(Fr,\ C_q,\ \sigma_c)$; case 2 $(B = 1.5\,\%,\ h^* = 0.5)$ versus case 3 $(B = 1.5\,\%,\ h^* = 0.17)$ in table 1.

https://doi.org/10.1017/jfm.2018.638 Published online by Cambridge University Press

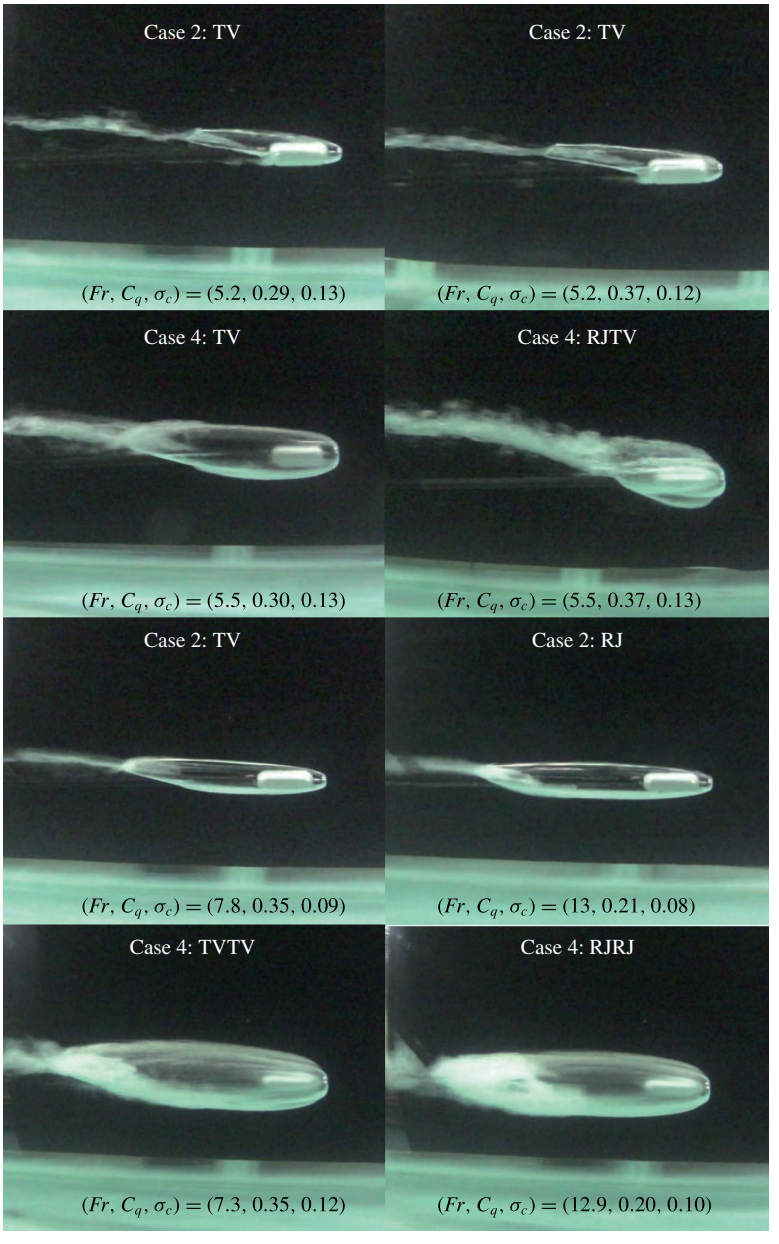

FIGURE 44. (Colour online) Side view observations of steady-state phenomena for similar values of $(Fr,\ C_q,\ \sigma_c)$; case 2 ($B = 1.5\,\%$, $h^* = 0.5$) versus case 4 ($B = 3\,\%$, $h^* = 0.5$) in table 1.

REFERENCES

CAMERON, P. J. K., ROGERS, P. H., DOANE, J. W. & GIFFORD, D. H. 2011 An experiment for the study of free-flying supercavitating projectiles. *Trans. ASME J. Fluids Engng* **133** (2), 021305.

CAMPBELL, I. J. & HILBORNE, D. V. 1958 Air entrainment behind artificially inflated cavities. In *Proc. of 2nd Symp. on Naval Hydrodynamics, Washington, DC*. Office of Naval Research.

https://doi.org/10.1017/jfm.2018.638 Published online by Cambridge University Press

CECCIO, S. L. 2010 Friction drag reduction of external flows with bubble and gas injection. *Annu. Rev. Fluid Mech.* **42**, 183–203.

COX, R. N. & CLAYDEN, W. A. 1956 Air entrainment at the rear of a steady cavity. In *Proc. of Symp. on Cavitation in Hydrodynamics, London*. National Physical Laboratory.

EPSHTEIN, L. A. 1973 Characteristics of ventilated cavities and some scale effects, unsteady water flow with high velocities. In *Proc. of IUTAM Symp. on Non-steady Flow of Water at High Speeds, Leningrad*. Nauka Publishing House.

FRANC, J. P. & MICHEL, J. M. 2004 *Fundamentals of Cavitation*. Kluwer Academic Publishers.

GADD, G. E. & GRANT, S. 1965 Some experiments on cavities behind disks. *J. Fluid Mech.* **23** (4), 645–656.

GARABEDIAN, P. R. 1955 Calculation of axially symmetric cavities and jets. *Pac. J. Maths.* **6** (4), 611–684.

GOLDSTEIN, S. 1938 *Modern Developments in Fluid Dynamics*. Oxford University Press.

HAALAND, S. E. 1983 Simple and explicit formulas for the friction factor in turbulent pipe flow. *Trans. ASME J. Fluids Engng* **105** (1), 89–90.

HAIPENG, W., SONG, F., QIN, W., BIAO, H. & GUOYU, W. 2014 Experimental and numerical research on cavitating flows around axisymmetric bodies. *J. Mech. Sci.* **28** (11), 4527–4537.

HRUBES, J. D. 2001 High-speed imaging of supercavitating underwater projectiles. *Exp. Fluids* **30** (1), 57–64.

KAPANKIN, Y. N. & GUSEV, A. V. 1984 Experimental research of joint influence of fluid and lift power of cavitator on character of flow in cavity rear part and gas departure from it. In *Proc. CAHI*, vol. 2244, pp. 19–28.

KARLIKOV, V. P., REZNICHENKO, N. T., KHOMYAKOV, A. N. & SHOLOMOVICH, G. I. 1987 A possible mechanism for the emergence of auto-oscillations in developed artificial cavitation flows and immersed gas jets. *Fluid Dyn.* **22** (3), 392–398.

KARN, A., ARNDT, R. E. A. & HONG, J. 2016 An experimental investigation into supercavity closure mechanisms. *J. Fluid Mech.* **789**, 259–284.

KAWAKAMI, E. 2010 Investigation of the behavior of ventilated supercavities. MS thesis, University of Minnesota, Twin Cities.

KAWAKAMI, E. & ARNDT, R. E. A. 2011 Investigation of the behavior of ventilated supercavities. *Trans. ASME J. Fluids Engng* **133** (9), 091305.

KUKLINSKI, R., HENOCH, C. & CASTANO, J. 2001 Experimental study of ventilated cavities on dynamic test model. In *CAV2001: Fourth Intl Symp. on Cavitation*, pp. 1–8. Naval Undersea Warfare Center.

LOGVINOVICH, G. V. 1972 *Hydrodynamics of Free-boundary Flows (Translated form Russian)*. IPST Press.

NOURI, N. M., MADOLIAT, R., JAHANGARDY, Y. & ABDOLAHI, M. 2015 A study on the effects of fluctuations of the supercavity parameters. *Exp. Therm. Fluid Sci.* **60**, 188–200.

PANTON, R. L. 2005 *Incompressible Flow*, 3rd edn. Wiley.

REICHARDT, H. 1946 The laws of cavitation bubbles at axially symmetrical bodies in a flow. *Rep. and Trans.* 35. Ministry of Aircraft Production, Great Britain.

SCHAFFAR, M., REY, C. & BOEGLEN, G. 2005 Behavior of supercavitating projectiles fired horizontally in water tank: theory and Experiments-CFD Computations with the OTi-Hull hydrocode. In *Proc. Thirty fifth AIAA Fluid Dynamic Conf. and Exhi., Toronto*, pp. 1–8.

SCHAUER, T. J. 2003 An experimental study of a ventilated supercavitating vehicle. MS thesis, University of Minnesota, Twin Cities.

SELF, M. W. & RIPKEN, J. F. 1955 Steady-state cavity studies in a free-jet water tunnel. *Rep.* 47. St. Anthony Fall Hydraulic Laboratory, University of Minnesota, Twin Cities.

SEMENENKO, V. N. 2001*a* *Artificial Supercavitation: Physics and Calculation*. Institute of Hydromechanics, National Academy of Sciences of Ukraine.

SEMENENKO, V. N. 2001*b* *Dynamic Processes of Supercavitation and Computer Simulation*. Institute of Hydromechanics, National Academy of Sciences of Ukraine.

SILBERMAN, E. & SONG, C. S. 1961 Instability of ventilated cavities. *J. Ship Res.* **5** (1), 13–33.

https://doi.org/10.1017/jfm.2018.638 Published online by Cambridge University Press

SKIDMORE, G. 2013 The pulsation of ventilated supercavities. Master of Science thesis, Department of Aerospace Engineering, Pennsylvania State University, University Park.

SONG, C. S. 1961 Pulsation of ventilated cavities. *Rep.* 32B. St. Anthony Fall Hydraulic Laboratory, University of Minnesota, Twin Cities.

SPURK, J. H. & KÖNIG, B. 2002 On the gas loss from ventilated supercavities. *Acta Mech.* **155**, 125–135.

SUMER, B. M. & FREDSOE, J 2010 *Hydrodynamics Around Cylindrical Structures*. World Scientific.

WAID, R. L. 1957 Cavity shapes for circular disks at angles of attack. *Rep.* E-73.4. Hydrodynamics Laboratory, California Institute of Technology, Pasadena.

WHITE, F. M. 1999 *Fluid Mechanics*, 4th edn. McGraw-Hill.

ZHOU, J., YU, K., MIN, J. & YANG, M. 2010 The comparative study of ventilated super cavity shape in water tunnel and infinite flow field. *J. Hydrodyn.* B **22** (5), 689–696.

https://doi.org/10.1017/jfm.2018.638 Published online by Cambridge University Press